Accepted Manuscript

New insight into the effect of fluorine doping and oxygen vacancies on electrochemical performance of Co_2MnO_4 for flexible quasi-solid-state asymmetric supercapacitors

Shude Liu, Ying Yin, Dixing Ni, Kwan San Hui, Ming Ma, Sewon Park, Kwun Nam Hui, Chu-Ying Ouyang, Seong Chan Jun

Please cite this article as: S. Liu, Y. Yin, D. Ni, K.S. Hui, M. Ma, S. Park, K.N. Hui, C.-Y. Ouyang, S.C. Jun, New insight into the effect of fluorine doping and oxygen vacancies on electrochemical performance of Co_2MnO_4 for flexible quasi-solid-state asymmetric supercapacitors, *Energy Storage Materials* (2019), doi: https://doi.org/10.1016/j.ensm.2019.02.014.

New Insight into the Effect of Fluorine Doping and Oxygen Vacancies on Electrochemical Performance of Co$_2$MnO$_4$ for Flexible Quasi-Solid-State Asymmetric Supercapacitors

Shude Liu,[1] Ying Yin,[1, 2] Dixing Ni,[3] Kwan San Hui,[4] Ming Ma,[5] Sewon Park,[1] Kwun Nam Hui,*[,6] Chu-Ying Ouyang,*[,3] and Seong Chan Jun*[,1]

[1]School of Mechanical Engineering, Yonsei University, Seoul 120-749, South Korea.

[2]Guangxi Key Laboratory of Information Materials, Guilin University of Electronic Technology, Guilin 541004, PR China.

[3]Department of Physics, Jiangxi Normal University, Nanchang, 330022, China.

[4]Engineering, Faculty of Science, University of East Anglia, Norwich, NR4 7TJ, United Kingdom

[5]Shenzhen Key Laboratory of Nanobiomechanics, Shenzhen Institutes of Advanced Technology, Chinese Academy of Sciences, Shenzhen 518055, Guangdong, China.

[6]Institute of Applied Physics and Materials Engineering, University of Macau, Avenida da Universidade, Taipa, Macau, China.

*Corresponding author's E-mail: bizhui@umac.mo; cyouyang@jxnu.edu.cn; scj@yonsei.ac.kr

New Insight into the Effect of Fluorine Doping and Oxygen Vacancies on Electrochemical Performance of Co_2MnO_4 for Flexible Quasi-Solid-State Asymmetric Supercapacitors

Abstract

Anion doping and oxygen-defect creation have been extensively employed to modify the electronic properties and increase concentration of electrochemically active sites of electrode materials for electrical energy storage technologies; however, comprehensive study of the roles of anion doping and oxygen vacancy on the enhancement of electrochemical performance is not clear. Herein, we provide new insight into the effect of fluorine dopant and oxygen vacancy on electrochemical performance of fluorine-doped oxygen-deficient Co_2MnO_4 (F-Co_2MnO_{4-x}) nanowires grown on carbon fiber (CF) as advanced electrode materials for supercapacitor. An experimental and theoretical study reveals that the structural and electronic properties in F-Co_2MnO_{4-x} is effectively tuned by introducing F dopants and oxygen vacancies, synergistically increasing electrical conductivity and providing rich Faradaic redox chemistry. The resultant F-Co_2MnO_{4-x} achieves a high specific capacity of 269 mA h g^{-1} at 1 A g^{-1}, and superior cyclic stability with 93.2% capacity retention after 5000 cycles at 15 A g^{-1}. A flexible quasi-solid-state asymmetric supercapacitor (ASC) is constructed with F-Co_2MnO_{4-x}/CF as the positive electrode and Fe_2O_3/CF as the negative electrode. The ASC device exhibits a high energy density of 64.4 W h kg^{-1} at a power density of 800 W kg^{-1}. Significantly, the device yields 89.9% capacitance

1

retention after 2000 bending tests at a bending angle ranging from 0 to 30°, demonstrating the high integration of excellent mechanical flexibility and cycling stability.

Keywords: fluorine doping; oxygen vacancies; Co_2MnO_4; flexible quasi-solid-state asymmetric supercapacitor; density functional theory calculations

1. Introduction

With the increasing demand for portable and wearable electronic devices, flexible supercapacitors have been developed because of their higher power density and longer cycling performance than those of lithium ion batteries (LIBs); however, their relatively lower energy density than those of LIBs impedes their practical applications [1, 2]. The improvement of energy density for supercapacitors can be achieved by increasing the specific capacitance or maximizing the cell voltage [3]. Recently, an effective approach that broadens the energy density of supercapacitors is to construct an asymmetric supercapacitor (ASC) by combining high capacity battery-type electrode and high rate capacitive electrode [4, 5]. In general, ASC devices are mostly operated in aqueous electrolytes, which easily suffer from solvent evaporation and possible leakage of harmful electrolytes [6, 7]. By contrast, quasi/all-solid-state ASC devices with gel electrolytes are preferred to avoid this problem and provide additional advantages, such as lightweight, high mechanical integrity, good reliability, and wide operating temperature [8, 9]. In this regard, solid-state ASC devices have been widely explored as an alternative to next-generation portable and flexible

2

electronics. However, studies have yet to overcome development of high-energy solid-state ASC devices without sacrificing their power density and life span.

Extensive research efforts have been devoted to the development of desirable battery-type materials (e.g., nickel and cobalt compounds) in electrochemical energy storage systems, such as supercapacitors, LIBs and rechargeable alkaline batteries owing to their high theoretical capacity, low cost, and abundance in nature [10-12]. Among them, cobalt manganese oxides with multiple oxidation states in particular are considered attractive because they combine the prominent features of the extremely high theoretical capacity of Co_3O_4 and high rate capability of MnO_2 [13]. Nevertheless, they still suffer from these disadvantages, such as low electrical conductivity, sluggish kinetics, and poor electrochemical stability, thus limiting their implementation in real applications. Very recently, substitutional anion-doping in transition metal oxides has been demonstrated as an effective approach to tune electrochemical and electrical properties of metal oxide electrodes [14]. Liang et al. reported that by incorporating fluorine (F) dopant in NiFe-based oxide electrode, remarkable specific capacitance of 670 F cm^{-3} (134 mF cm^{-2}) can be achieved [15]. Previous density functional theory (DFT) studies showed that the substitution of F for O in Fe_2O_3 improves electrical conductivity because of the generation of defect levels and the decreased band gap after F dopants, thereby facilitating the reaction kinetics of Fe_2O_3 toward a photoelectrochemical processes [16]. In addition, the highly ionic nature of the metal-fluorine bond that can provide higher lattice energy and suppress the polarization with respect to their oxide counterparts, and thus increases redox

3

potential of electrode materials [17, 18]. On the other hand, the intentional creation of O vacancies in the lattice of transition metal oxides has been proven as an effective approach to increase the reactivity of electrochemically active sites and to modify electrical properties [19, 20], which are beneficial to enhancement of electrochemical performance. Kim et al. [21] reported that O vacancy-induced α-MoO_3 efficiently increased the carrier concentration and promoted a faster charge storage kinetics than those of fully oxidized α-MoO_3, thereby remarkably enhancing electrochemical performance. However, the combined effects of F dopant and O vacancies on the electronic structure and electrochemical properties of transition metal oxides in energy storage systems have been rarely studied.

Herein, we report an effective strategy to boost the electrochemical performance of F-Co_2MnO_{4-x} nanowires grown on carbon fiber (CF) as excellent electrode materials for supercapacitor through introducing F heteroatoms and O vacancies. The enhanced electrochemical performances of F-Co_2MnO_{4-x} nanowires are comprehensively studied by theoretical calculations and experimental analyses. The resultant F-Co_2MnO_{4-x}/CF exhibits high specific capacity and good cyclic stability. Moreover, a flexible quasi-solid-state asymmetric supercapacitor (ASC) with F-Co_2MnO_{4-x}/CF as the positive electrode and Fe_2O_3/CF as the negative electrode yields a high energy density of 64.4 W h kg^{-1} at a high power density of 800 W kg^{-1}. This ASC device also retains 24.2 W h kg^{-1} even at an ultrahigh power density of 8000 W kg^{-1} and a long cycling life (95.4% capacitance retention after 5000 cycles). In addition, the

4

device shows 89.9% retention of the initial specific capacitance at 10 mV^{-1} over 2000

bending cycles at a bending angle from 0° to 30°.

2. Results and Discussion

2.1 Characterization and electrochemical properties of the positive electrode material

The detailed schematic procedure of F-Co$_2$MnO$_{4-x}$ nanowires is illustrated in Fig. 1a.

The F-Co$_2$MnO$_4$ precursor nanowires grown on the CF substrate were prepared via a

hydrothermal reaction. Co^{2+} and Mn^{2+} are firstly hydrolyzed and lead to in-situ

deposition of F-Co$_2$MnO$_4$ precursor on growth substrate after consecutive nucleation

and crystal growth stages. SEM images show that the entire surface of the CF

substrate is covered by densely packed precursor nanowires with a diameter of 100–

200 nm and a length of 2–3 μm (Fig. 1b, c and S1). The phase of the precursor was

investigated through XRD analysis (Fig. S2), which is matched with the reported

layered double hydroxides (LDHs) phase [22]. In LDHs structure, the partial bivalent

metal cations coordinated octahedrally by hydroxyl groups are substituted by the

isomorphous trivalent metal cations, leading to the formation of positively charged

layers [23, 24]. Therefore, the F anions derived from the reactant NH$_4$F during the

hydrothermal synthesis are inserted as interlayer anions between positively charged

host layers of Co-Mn LDHs for balancing charge [24]. Then, F-Co$_2$MnO$_4$ is obtained

by annealing Co-Mn LDHs in air at 350 °C for 2 h, in which partial O sites are

substituted by F dopants. The morphological shape of the F-Co$_2$MnO$_4$ nanowires is

maintained after calcination (Fig. 1d and S3a–c). SEM analysis reveals that none-doped Co_2MnO_4 preserves almost unanimous morphology relative to F-doped Co_2MnO_4 (Fig. S3d–f). Careful observation reveals that the nanowires are composed of abundant highly crystalline nanoparticles, which are attributed to the release of H_2O and CO_2 gases during the thermal decomposition of the precursor. The SEM image and its corresponding energy dispersive spectrometry (EDS) elemental mapping images (Fig. S4a–e) clearly display the presence of Co, Mn, O, and F in the F-Co_2MnO_4 nanostructure, agreeing with the EDS spectrum (Fig. S4f). Finally, F-Co_2MnO_4 was treated with NaOH dissolved in ethylene glycol (EG) for solvothermal process. EG, a reductant in an alkaline medium, provides a mild reduction condition to chemically reduce metal oxides and potentially create O vacancies without destroying crystalline/microstructure [10]. As a result, F-Co_2MnO_{4-x} is obtained through the solvothermal reduction. Fig. 1e and S3g–i show that the morphology and alignment of the nanowires are well preserved after the reduction. However, the surface of the F-Co_2MnO_{4-x} nanowires becomes rough possibly because of the etching effect and chemical reduction. This unique nanoarchitecture of F-Co_2MnO_{4-x} is further demonstrated by the SEM-EDS elemental mappings of Co, Mn, O, and F (Fig. S5a–e). The corresponding EDS spectrum (Fig. S5f) shows that the stoichiometric ratio of Co:Mn:O:F is about 2.01:1.00:3.30:0.12 in F-Co_2MnO_{4-x} sample. Accordingly, the x value in F-Co_2MnO_{4-x} is determined to ~0.53. The mass ratio of the detected F (1.81 at.%) slightly changes after reduction, indicating that F is stable during the solvothermal process.

6

TEM was performed to investigate the detailed structural information of F-Co$_2$MnO$_{4-x}$. Consistent with the SEM results, the low-dimension TEM image shows that the nanowires consist of numerous connected nanocrystals with sizes of 5–10 nm (Fig. 2a, b). The high-resolution TEM (HRTEM) image (Fig. 2c) reveals clear lattice fringes of 0.294 and 0.249 nm that correspond to the d-spacings of (200) and (311) planes of Co$_2$MnO$_4$, respectively. The selected area electron diffraction (SAED) pattern of F-Co$_2$MnO$_{4-x}$ shows clear diffraction rings (Fig. 2d), which can be ascribed to (111), (220), (311), (400), (511), and (440) planes of Co$_2$MnO$_4$. A representative STEM image of F-Co$_2$MnO$_{4-x}$ and its corresponding EDS elemental mappings show that all of the elements are distributed homogeneously throughout the nanowires (Fig. 2e–i).

The crystallographic structures of the as-made products were examined through XRD analysis. For the XRD patterns of Co$_2$MnO$_4$, F-Co$_2$MnO$_4$, and F-Co$_2$MnO$_{4-x}$ samples (Fig. S7a), except the patterns of the broad peaks at 2θ of ~26.2° and 44.1° attributed to the CF substrate, all of the other diffraction peaks are assigned to cubic Co$_2$MnO$_4$ with the space group Fd$\bar{3}$m (JCPDS No. 01-1130), indicating that the introduction of F atoms or O vacancies did not cause phase transition. The decrease of the peak intensities upon the introduction of F heteroatoms and O vacancies into Co$_2$MnO$_4$ is attributed to the slight degradation of the crystallinity, which is due to the disruption of the crystal lattice structure from introduced defect within typical samples. Notably, the (220) diffraction peak of F-Co$_2$MnO$_4$ at around 2θ=31.5° is observed to shift slightly toward lower angles relative to pristine Co$_2$MnO$_4$, indicating that the lattice volume increases as a result of the introduction of F heteroatoms, which is consistent

7

with previous report [25]. The Raman spectra were carried out to investigate the bonding characteristic of the as-synthesized samples (Fig. S7b). For Co_2MnO_4, the conspicuous peaks observed at 189, 476, 517, and 680 cm^{-1} are assigned to F_{2g}, E_g, F_{2g}, and A_{1g} models of Co_2MnO_4, respectively, and this assignment is consistent with previous reports [26, 27]. Compared to those of pristine Co_2MnO_4 and $F-Co_2MnO_4$, the scissoring vibration F_{2g} at 189 cm^{-1} in the Raman spectrum of $F-Co_2MnO_{4-x}$ disappears [28], which is possibly due to disruption of crystalline symmetry as a result of increased O vacancies within the nonstoichiometric $F-Co_2MnO_{4-x}$ matrix. In comparison with the peaks of Co_2MnO_4, the Raman peaks of $F-Co_2MnO_4$ and $F-Co_2MnO_{4-x}$ slightly shift to a higher wavenumber, which is ascribed to a large unit cell as a result of partial F substitution for O. No additional signals can be detected, indicating the complete conversion of the precursor to metal oxide after annealing. To examine the effect of solvothermal reduction on the intrinsic defect of $F-Co_2MnO_{4-x}$, we conducted electron paramagnetic resonance (EPR) to probe the O vacancy (**Fig. 3**a). All of the samples show a symmetrical signal at the magnetic field corresponding to $g = 1.95$, indicating that presence of O vacancies in the lattice, and this observation agrees with a previous report [29, 30]. It can be observed that the EPR intensity of $F-Co_2MnO_{4-x}$ is much larger than those of Co_2MnO_4 and $F-Co_2MnO_4$, suggesting that more O vacancies are created in $F-Co_2MnO_{4-x}$ [31].

XPS was conducted to investigate the surface chemical compositions of Co_2MnO_4, $F-Co_2MnO_4$, and $F-Co_2MnO_{4-x}$. The surface atomic ratios obtained from XPS analysis are listed in Table S1. The Co $2p$ spectrum of Co_2MnO_4 can be divided into two

8

spin-orbit doublets and two shake-up satellites (Fig. 3b), which are characteristics of Co^{3+} and Co^{2+} [32]. A positive shift in the peaks of F-Co_2MnO_4 is observed compared with that of Co_2MnO_4, thereby supporting the incorporation of a more electronegative F that draws an electron from Co in the lattice; as a result, the binding energy increases. However, the Co $2p$ peaks of F-Co_2MnO_{4-x} are positively shifted relative to F-Co_2MnO_4, indicating the formation of more Co^{2+} in F-Co_2MnO_{4-x} [33, 34] because of the partial reduction of Co^{3+} and the increased concentration of O vacancies [34]. Compared to Co_2MnO_4, the two satellite peaks corresponding to the Co^{2+} of the F-Co_2MnO_4 and F-Co_2MnO_{4-x} at about 786.5 eV and 802.8 eV are swelled [35], which is attributed that a portion of Co^{3+} ions is reduced to Co^{2+} with generating F heteroatoms and O vacancies. The finding indicates the increased atomic ratio of Co^{2+}/Co^{3+} on the surface of the typical samples. The Mn $2p$ spectrum of Co_2MnO_4 shows Mn $2p_{3/2}$ and Mn $2p_{1/2}$ peaks located at 641.8 and 653.5 eV, respectively (Fig. 3c). The fitting peaks at 643.2 and 652.7 eV are indexed to Mn^{3+}, while the other peaks at 644.2 and 665.4 eV can be identified as Mn^{2+} [36]. Consistent with the case of Co $2p$ peaks, the peaks in Mn $2p$ of F-Co_2MnO_4 and F-Co_2MnO_{4-x} shift slightly to a lower energy level compared with those of Co_2MnO_4, implying that more Mn^{2+} form as induced by F dopants and O vacancies. It is noted that the atomic ratio of M^{2+}/M^{3+} (M presents Co and Mn) for F-Co_2MnO_{4-x} is higher than that for Co_2MnO_4, which agrees with the relatively more F dopants and O vacancies within F-Co_2MnO_{4-x}. The appearance of F $1s$ peak at around 683.9 eV corresponds to the characteristic of F-metal bond, verifying the successful incorporation of F into Co_2MnO_4 (Fig. 3d) [37,

38]. The atomic contents of F in F-Co_2MnO_4 and F-Co_2MnO_{4-x} as determined by XPS analysis are 2.08% and 1.92%, respectively (Table S1), which are similar to the bulk F ratio measured through EDS. This finding elucidates the uniform distribution of F throughout the F-Co_2MnO_{4-x} nanostructure. For the O 1s core-level spectrum, the peaks shift to a higher binding energy after a highly electronegative F is incorporated into the lattice possibly because of the large electron-withdrawing effect of cations coordinated with F (Fig. S8) [39]. The partial substitution of lattice O^{2-} with F^- can increase the amount of low valence Co^{2+} and Mn^{2+} ions to compensate the charge imbalance. The generation of low valence cations could further facilitate the electron conduction due to mixed valence electron hopping, which enables efficient electrode kinetics and thus increases electrochemical performance [40]. Conversely, the O 1s spectrum of F-Co_2MnO_{4-x} shifts to a lower binding energy compared with that of F-Co_2MnO_4, implying a weakened metal−O bond caused by surface O defects [19]. The O vacancies have been proven to facilitate intrinsic conductivity and electrochemical redox activity [20, 41]. Therefore, the F-Co_2MnO_{4-x} with abundant O vacancies is expected to achieve good electrochemical properties in supercapacitors.

The electrochemical properties of the as-made samples as electrode materials were evaluated in a three-electrode configuration by using 1 M KOH as the aqueous electrolyte. Fig. 4a shows the comparison of the typical CV curves of Co_2MnO_4/CF, F-Co_2MnO_4/CF, and F-Co_2MnO_{4-x}/CF electrodes at a scan rate of 30 mV s^{-1} with a potential window within 0–0.6 V versus the saturated calomel electrode (vs. SCE). The CV curves of the entire samples reveal a pair of pronounced redox peaks, which

correspond to the possible the reversible Faradaic redox reactions. The reactions could be expressed by the following equations [26, 42, 43].

$$Co_2MnO_4 + H_2O + OH^- \rightleftharpoons MnOOH + 2CoOOH + e^- \qquad (1)$$

$$CoOOH + OH^- \rightleftharpoons CoO_2 + H_2O + e^- \qquad (2)$$

$$MnOOH + OH^- \rightleftharpoons MnO_2 + H_2O + e^- \qquad (3)$$
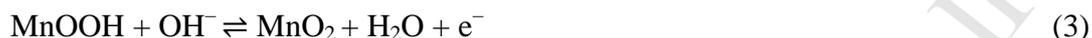
The areal current response of the bare CF substrate is much smaller than those of Co_2MnO_4/CF, F-Co_2MnO_4/CF, and F-Co_2MnO_{4-x}/CF electrodes (Fig. S9), indicating its negligible contribution to the charge storage. The CV integral area of F-Co_2MnO_{4-x}/CF electrode is larger than that of Co_2MnO_4/CF and F-Co_2MnO_4/CF electrodes at the same scan rate, indicating the highest specific capacity. The continuously improved electrochemical performance of F-Co_2MnO_{4-x} may be attributed to the formed low valence Co^{2+} and Mn^{2+} ions within typical sample as a result of the introduction of F dopants and O vacancies. Moreover, the CV curves of F-Co_2MnO_{4-x}/CF obtained at different scan rates ranging from 5 mV s^{-1} to 50 mV s^{-1} have no obvious deformation (Fig. 4b), revealing small ohmic resistance and polarization [44]. To further investigate the charge storage kinetics of F-Co_2MnO_{4-x}/CF electrode, we analyzed the dependence of the current density (I) on the scan rate (v) by using $I = a \cdot v^b$ [45], where a and b are variable constants. b is determined from the slope of a plot of log(i) versus log(v) (Fig. 4c). If b is 1, then the reaction kinetics is a characteristic of the capacitive process; if b is 0.5, then the reaction kinetics is diffusion controlled. Our results reveal b of 0.527 and 0.532 at the

11

potentials of the anodic and cathodic peaks, respectively, and these values are close to

0.5, indicating that the peak current contribution primarily originates from diffusion

processes. The current response can be quantized by separating the contributions of

capacitive and diffusion-controlled processes at a fixed potential at $i = k_1v + k_2v^{1/2}$ (Fig.

4d) [46], where k_1 and k_2 are the coefficients in the capacitor-like and diffusion

processes, respectively. The ratio of capacitive charge storage to the total charge

increases as scan rate increases. The fraction of the non-Faradaic capacity is

determined to ~12% at the lowest scan rate of 5 mV s^{-1}, suggesting a dominant

diffusion-controlled process of F-Co$_2$MnO$_{4-x}$, and this observation is consistent with

natural battery-type materials [47, 48].

The galvanostatic charge-discharge (GCD) curves of Co$_2$MnO$_4$/CF, F-Co$_2$MnO$_4$/CF,

and F-Co$_2$MnO$_{4-x}$/CF electrodes were performed in the potential window of 0–0.45 V

(vs. SCE) at a current density of 1 A g^{-1}. In Fig. 4e, the discharging time of

F-Co$_2$MnO$_4$/CF and F-Co$_2$MnO$_{4-x}$/CF electrodes is longer than that of Co$_2$MnO$_4$/CF,

and F-Co$_2$MnO$_{4-x}$/CF presents the longest discharging time. The GCD curves of the

F-Co$_2$MnO$_{4-x}$/CF electrode at different current densities are approximately symmetric,

indicating good electrochemical reversibility (Fig. 4f). Consistent with the CV results,

the plateau in the GCD curves illustrates the dominant charge storage mechanism of

Faradaic redox processes [49]. Considering that the GCD plots of all of the samples

are nonlinear and associated with the noncapacitive Faradaic behavior of battery-type

materials, we should apply the area integration of the GCD curves to provide the most

precise way of charge storage analysis (details in experimental section) [4]. The

longer discharge plateau of the F-Co_2MnO_{4-x} relative to the other samples further manifests that the introduced F atoms and O vacancies play a vital role in the charge–discharge properties. The calculated specific capacity as a function of discharge current density is plotted in Fig. 4g. The specific capacities of Co_2MnO_4/CF, F-Co_2MnO_4/CF, and F-Co_2MnO_{4-x}/CF at a current density of 1 A g^{-1} are 165, 204, and 269 mA h g^{-1}, respectively. The F-Co_2MnO_{4-x}/CF electrode also highly exceeds the capacity values of CoMn-based ternary oxides [26, 50-52]. F-Co_2MnO_4/CF and F-Co_2MnO_{4-x}/CF electrodes show a higher rate capability (higher than 56.3% of the initial specific capacity) than Co_2MnO_4/CF electrode (~50.1%) as current density increases from 1 A g^{-1} to 15 A g^{-1}. The feasibility analysis of rate capability retentions for the samples prepared in three independent experiments was studied. The intermediate value of rate capability retentions at different batches electrodes shows small deviation within ± 3.4% (Fig. S10), revealing good repeatability of electrode performance. Correspondingly, the areal capacities of Co_2MnO_4, F-Co_2MnO_4 and F-Co_2MnO_{4-x} at a current density of 1 mA cm^2 were determined to be 0.228, 0.295 and 0.366 mA h cm^{-2}, respectively (Fig. S11). Furthermore, F-Co_2MnO_{4-x} still retains the areal capacity of 0.223 mA h cm^{-2} even at a high current density of 15 mA cm^{-2}, which is higher than those of Co_2MnO_4 (0.119 mA h cm^{-2}) and F-Co_2MnO_4 (0.171 mA h cm^{-2}). The BET specific surface areas recorded from powders of the synthesized Co_2MnO_4-based nanostructures were evaluated from N_2 adsorption–desorption isotherm. The N_2 sorption isotherms exhibit a typical type-IV curve with obvious hysteresis loops at the P/P_0 ranges of 0.5–1.0 (Fig. S6), indicating

13

the existence of mesoporous structures within typical samples [53]. The specific surface areas of Co_2MnO_4, $F-Co_2MnO_4$ and $F-Co_2MnO_{4-x}$ powder samples are estimated to be 43.8, 47.9, and 57.4 m^2 g^{-1}, respectively. The areal capacity of $F-Co_2MnO_{4-x}$ normalized relative to its BET specific surface area at 1 A g^{-1} was calculated to be 4.7 mA h m^{-2}, which is larger than that of $F-Co_2MnO_4$ (4.3 mA h m^{-2}) and Co_2MnO_4 (3.8 mA h m^{-2}). The enhanced areal capacity for $F-Co_2MnO_{4-x}$ can be attributed to the tuned electrical structure and improved electrochemical activity after introducing F atoms and O vacancies. To clarify whether simultaneous introduction of F dopants and O vacancies can indeed improve the electrical conductivity of pure Co_2MnO_4, the four-probe technique was carried out to measure the conductance. The electrical conductivity obtained for $F-Co_2MnO_{4-x}$ is 9.1×10^{-2} S m^{-1}, which is significantly improved in comparison to that of Co_2MnO_4 (7.6×10^{-3} S m^{-1}) and $F-Co_2MnO_4$ (4.2×10^{-2} S m^{-1}).

The electrochemical impedance spectroscopy (EIS) measurements of the as-made samples were carried out to analyze the cause of the enhanced performance. The EIS spectra of all of the samples exhibit a semicircle in the high-frequency region corresponding to charge transport resistance (R_{ct}) induced by the redox reactions at the electrode/electrolyte interface, and a straight line in the low-frequency region related to the diffusive resistance of the electrolyte (Warburg impedance). The intercept of the EIS curve on the real axis represents the equivalent series resistance (R_s), which includes the intrinsic resistance of an active material, the electrolyte resistance, and interface resistance between the current collector and the active

14

material. In Fig. S12, R_s of F-Co$_2$MnO$_{4-x}$/CF electrode is 0.6 Ω, which are lower than those of F-Co$_2$MnO$_4$/CF (0.7 Ω) and Co$_2$MnO$_4$/CF (0.9 Ω). Moreover, R_{ct} of F-Co$_2$MnO$_{4-x}$/CF is 1.4 Ω, which is smaller than those of F-Co$_2$MnO$_4$/CF (4.8 Ω) and Co$_2$MnO$_4$/CF (7.9 Ω). The results indicate improved electrical conductivity and accelerated reaction kinetics of F-Co$_2$MnO$_{4-x}$/CF. These findings again demonstrate the improvement of electrical conductivity and charge transfer kinetics after introducing F atoms and O vacancies. The cycling stabilities of the prepared electrodes were investigated at a high current density of 15 A g^{-1} (Fig. 4h). After 5000 cycles, Co$_2$MnO$_4$/CF, F-Co$_2$MnO$_4$/CF, and F-Co$_2$MnO$_{4-x}$/CF maintain 85.8%, 90.9%, and 93.3% of the initial capacity, respectively. This capacity retention of F-Co$_2$MnO$_{4-x}$/CF is substantially higher than those of transition metal-based nanostructures [54-56]. Notably, all electrodes exhibit Coulombic efficiencies beyond 98% during cycling test (Fig. S13), implying their highly reversible redox reactions. Furthermore, a slight increase in R$_s$ and R$_{ct}$ is observed in F-Co$_2$MnO$_{4-x}$ electrode after 5000 GCD cycles (Fig. S14), which is ascribed to the robust interfaces of nanomaterials and conductive CF substrate. Clearly, F-Co$_2$MnO$_{4-x}$ shows lower R$_s$ and R$_{ct}$ than those of pristine Co$_2$MnO$_4$ and F-Co$_2$MnO$_4$, indicating better electrical conductivity and faster kinetics of F-Co$_2$MnO$_{4-x}$, which is probably due to the introduction of F dopants and O vacancies. To compare the electrochemical performance of the synthesized electrodes at full specific capacity, the cycling behavior of the synthesized electrodes was performed at a current density of 1 A g^{-1}. Clearly, the F-Co$_2$MnO$_{4-x}$/CF electrode possesses 97.4 % capacity retention after 1000

15

cycles, which is higher than F-Co$_2$MnO$_4$/CF (94.5 %) and Co$_2$MnO$_4$/CF (92.8 %) (Fig. S15). The finding suggests that the F-doping and O vacancies within nanostructures would contribute to the improvement of cycling stability. To probe the existence of the F dopant and O vacancy in the F-Co$_2$MnO$_{4-x}$ despite the phase transformation from metal oxide to metal oxyhydroxide during the redox reaction, SEM–EDS mapping and EPR spectrum of the cycled F-Co$_2$MnO$_{4-x}$ electrode at a current density of 15 A g^{-1} were characterized. The elemental mapping analysis of the 1000th cycled F-Co$_2$MnO$_{4-x}$ clearly reveals the existence of Co, Mn, O and F elements with Co/Mn/O/F atomic ratio of 1.96:1.00:3.51:0.11 (Fig. S16), which is very close to atomic content of initial F-Co$_2$MnO$_{4-x}$ (Fig. S5f). The finding reveals the good structural stability of F-Co$_2$MnO$_{4-x}$ during electrochemical cycling. Meanwhile, the peak intensity of EPR spectrum of the F-Co$_2$MnO$_{4-x}$ decreases gradually with increasing number of cycles (100, 1000, 3000 and 5000). However, the peak intensity of EPR spectrum of the 5000th cycled F-Co$_2$MnO$_{4-x}$ remains higher than that of F-Co$_2$MnO$_4$ (Fig. S17). The finding suggests that O vacancies still exist in F-Co$_2$MnO$_{4-x}$ during the consecutive Faradaic redox processes. To further confirm the presence of F dopant in the lattice of F-Co$_2$MnO$_{4-x}$ after 1000 cycles at 15 A g^{-1}, XPS measurement of 1000 cycled F-Co$_2$MnO$_{4-x}$ was performed. Results show that there is no obvious change in F 1s XPS spectrum before and after the cycling process (Fig. S18). The peak located at ~683.9 eV can be ascribed to the existence of F-metal bonds in the cycled F-Co$_2$MnO$_{4-x}$. All of these observations manifest that the greatly enhanced electrochemical properties of F-Co$_2$MnO$_{4-x}$ are attributed to continuous

16

improvement of the electrode kinetics as a result of introduction of F doping followed by creation of O vacancies.

DFT calculations were performed to investigate the role of F anions and O vacancies in the structural and electronic properties of Co_2MnO_4. Studies have shown that the ground state structure of Co_2MnO_4 is thermodynamically stable when it is an inverse spinel [57, 58]. In particular, Mn prefers to occupy the octahedral sites and exhibits as high-spin Mn^{3+} while half Co takes the tetrahedral sites as high-spin Co^{2+} and the other half takes the octahedral sites as nonmagnetic Co^{3+} [57]. Therefore, the structural and electronic analyses of Co_2MnO_4, Co_2MnO_{4-x}, $F-Co_2MnO_4$, and $F-Co_2MnO_{4-x}$ were performed on the basis of the inverse spinel model. For the F-doped case, we replaced 1 of the 32 O atoms with an F atom in the Co_2MnO_4 unit cell. To create O vacancy, we removed 1 of the 32 O atoms in the Co_2MnO_4 unit cell (Fig. S19). Table S2 presents the optimized lattice constants of F-doped and O vacancy-defected Co_2MnO_4 obtained from DFT calculations. To evaluate the thermodynamics of O vacancy formation and F doping, we calculated the O vacancy formation energy (E_{form}) and F doping energy (E_{dop}) within a unit cell as follows:

$$E_{form} = E(Co_2MnO_{4-x}) + 0.5xE(O_2) - E(Co_2MnO_4), \qquad (4)$$

$$E_{dop} = E(Co_2MnO_{4-x}F_x) - E(Co_2MnO_4) + 0.5xE(O_2) - 0.5xE(F_2), \qquad (5)$$

where $E(Co_2MnO_4)$, $E(Co_2MnO_{4-x})$, and $E(Co_2MnO_{4-x}F_x)$ are the calculated total energies of Co_2MnO_4, Co_2MnO_{4-x} and $F-Co_2MnO_{4-x}$, respectively; and $E(O_2)$ and $E(F_2)$ are the total energies of O_2 and F_2 in vacuum, respectively. From these definitions,

17

negative E_{dop} and low E_{form} correspond to favorable doping thermodynamics and vacancy formation, respectively. The calculated O vacancy formation energy is about 3.05 eV, which is quite high for intrinsic O vacancy formation. However, as the prepared samples are nanostructures, O vacancy formation at surfaces can be more favorable. Furthermore, the calculated E_{dop} is approximately –0.56 eV, indicating that F dopants can be created from a thermodynamic perspective.

The density of states (DOSs) of Co_2MnO_4, Co_2MnO_{4-x}, F-Co_2MnO_4, and F-Co_2MnO_{4-x} are given in Fig. 5. Impurity states are found in the forbidden band around the Fermi level (E_f) when F dopants and O vacancies are created. These impurity states decrease the band gap of the pure Co_2MnO_4 (Fig. 5 and Table S2). The band gap of Co_2MnO_4 is 0.35 eV. For Co_2MnO_{4-x}, F-Co_2MnO_4 and F-Co_2MnO_{4-x}, the band gaps decrease to 0.18, 0.14 and 0.13 eV, respectively. The decrease in the band gap induces an increase in electronic conductivity and provides enhanced reaction kinetics. This finding is consistent with the experimental observations (Fig. 4). The obtained band gap of the Co_2MnO_4 (0.35 eV) is in good agreement with other theoretical results ranging from 0 eV to 0.5 eV, which were calculated with different theoretical levels [13, 57, 59]. However, the energy gap of the Co_2MnO_4 seems too small comparing with the experimental observations, which ranges from 1.69 eV to 2.93 eV from different researchers [60-62]. We mention here that all these experimental results were obtained from fitting the UV-Vis absorption spectra [60-62], from which the energy gap represents only the optical transition between the conduction band and the valence band. However, there are many impurity states

18

staying in between the conduction band and the valence band (Fig. 5a), which are not sensitive to the UV-Vis absorption spectra. Without considering these impurity states, the energy gap between the valence band and the conduction band is larger than 2 eV, as can be seen in Fig. 5a.

The further analysis of the partial DOS (PDOS, Figure 5b, d, f, h) of the $3d$ states of different metal atoms shows that the energy states around the Fermi level are mainly contributed by the $3d$ states from Mn and Co atoms, particularly contributed by Mn^{2+} ions. Fig. S20 presents the band structure of $F-Co_2MnO_{4-x}$ and the band-decomposed charge density of the highest occupied band (highlighted in red in the inset in Fig. S20). The highest occupied band is composed of the $3d$ states of the low oxidation state Mn^{2+} ion, with a small contribution from the neighboring O atoms. These impurity states contribute to the electronic conductivity of Co_2MnO_4, as already mentioned above. The PDOS data further demonstrate that F dopants and O vacancies are beneficial to produce low valence state of Mn^{2+} and Co^{2+} ions. More importantly, the energy levels of the electronic states of these low oxidation state ions are very close to the Fermi level such that these states are very active upon electrochemical cycling, and thus enable rapid reaction kinetics of electrode materials. In the charging process, electrons taking these states near the Fermi level could be first transferred, and these low oxidation state Co^{2+} and Mn^{2+} ions dominantly change into Co^{3+} and Mn^{3+}, which further contribute to rich Faradic redox reactions [41, 63, 64].

2.2 Characterization and electrochemical properties of the negative electrode

19

material

Fig. 6a illustrates the typical synthesis of hollow Fe_2O_3 core-branch nanostructures on a CF substrate. The ZnO nanorods were initially synthesized via the seeded substrate and then subjected to a low-temperature hydrothermal process. The CF was fully covered with the aligned ZnO nanorods with diameters of 200–400 nm and lengths of 2–3 μm (Fig. S21a, b). The SEM-EDS elemental mappings and their corresponding EDS spectra confirm that Zn and O are uniformly distributed (Fig. S21c–f). The obtained ZnO nanorods are chosen as a sacrificial template, which is decomposed in the acid medium produced through Fe^{3+} precursor hydrolysis, whereas the dissolution of ZnO accelerates Fe^{3+} hydrolysis. After a shape-reservation transformation of the annealing treatment occurred under Ar, the well-oriented hollow Fe_2O_3 nanorods with decorated outer surfaces are finally obtained (Fig. 6b and c and Fig. S22). In Fig. 6d, a well-resolved lattice spacing of 0.372 nm corresponding to the (012) plane of Fe_2O_3 is observed. The crystallographic structure is confirmed in the XRD profile (Fig. S23a). All of the reflected peaks are indexed to the rhombohedral hematite phase (JCPDS No. 33-664), but the two other characteristic graphitic peaks are ascribed to the CF substrate. EDS elemental mappings show that Fe and O are homogeneously distributed in an individual tubular nanostructure (Fig. 6e-h). XPS analysis was carried out to further clarify the elemental composition and chemical state of the surface species. The full XPS spectrum of Fe_2O_3 (Fig. S23b) shows the existence of Fe and O, which are in accordance with the EDS analysis. The Fe $2p$ XPS spectrum (Fig. S23c) shows that the fitting peaks at 711.0 and 724.3 eV correspond to Fe $2p_{3/2}$

and Fe $2p_{1/2}$, respectively, along with two satellite peaks, which are consistent with the binding energies of Fe^{3+} in the reported Fe_2O_3 [65, 66]. The O $1s$ spectrum (Fig. S23d) can be deconvoluted into two characteristic peaks of O^{2-} derived from Fe_2O_3 (529.9 eV) and hydroxyl groups or surface-adsorbed O (531.5 eV) in accordance with previous report [67].

The electrochemical performance of as-synthesized Fe_2O_3/CF electrode for supercapacitor was evaluated with a three-electrode configuration in 1 M KOH electrolyte. Fig. S24a shows the CV curves obtained at scan rates ranging from 5 mV s^{-1} to 50 mV s^{-1} in a potential window of -1 V to 0 V (vs. SCE). The shape of the CV curves can be retained at different scan rates, implying good capacitive behavior. According to the CV shapes, it is indicated that the stored energy of Fe_2O_3/CF electrode is attributed to the electric-double layer capacitance by surface adsorption of electrolyte OH^- ions and the pseudocapacitance by Faradaic redox reaction of Fe^{2+}/Fe^{3+} [67]. The GCD curves of Fe_2O_3 at different current densities are almost linear and symmetric (Fig. S24b), revealing a highly reversible response and a good rate capability. The specific capacitance calculated from the GCD curves reaches 322 F g^{-1} at of 1 A g^{-1} (Fig. S24c), and this values exceeds that of Fe_2O_3 nanostructures [67, 68]. The specific capacitance of 124 F g^{-1} is retained even at a large current density of 15 A g^{-1}, implying a good rate capability. The cycling performance was evaluated at a current density of 8 A g^{-1} (Fig. S24d). After 5000 cycles, a capacitance retention of 87.8% with a Coulombic efficiency of 98.1% is obtained, indicating good cycling stability. R_s and R_{ct} obtained from the Fe_2O_3/CF electrode are ~1.1 and ~1.4 Ω,

respectively (Fig. S24e). No obvious changes can be observed in the EIS plots before and after the cycling test, and this phenomenon can be beneficial to a good electrochemical behavior. These excellent electrochemical performances can be attributed to the structural merits of Fe_2O_3/CF electrode (Fig. S24f).

2.3 Electrochemical performance of F-Co_2MnO_{4-x}/CF//Fe_2O_3/CF flexible quasi-solid-state ASC device

To further demonstrate the feasibility of F-Co_2MnO_{4-x}/CF//Fe_2O_3/CF for practical applications, we assembled ASC device by using F-Co_2MnO_{4-x}/CF as the positive electrode, Fe_2O_3/CF as the negative electrode, and filter paper as the separator with a KOH/PVA gel electrolyte (Fig. 7a). According to the comparative CV curves of Fe_2O_3/CF and F-Co_2MnO_{4-x}/CF obtained at a scan rate of 5 mV s^{-1} (Fig. S25a), the mass ratio of Fe_2O_3 to F-Co_2MnO_{4-x} is set to around 0.42 in the assembled ASC in accordance with the principle of charge balance [47]. Fig. S25b shows the CV curves of an optimized device at different voltage windows. The presence of the redox peaks is attributed to the reversible Faradaic reactions of the electrode materials. As the cell voltage of the ASC increases, the corresponding stored energy increases. The stable electrochemical window of the device can be extended to 1.6 V. However, the voltage window is increased to 1.7 V, the CV curve becomes slightly distorted. Thus, the optimized voltage window is determined to be 1.6 V for the ASC device.

The CV curves of the F-Co_2MnO_{4-x}/CF//Fe_2O_3/CF ASC were obtained at different scan rates ranging from 5 mV s^{-1} to 50 mV s^{-1} (Fig. 7b). No obvious deformation in

the CV curves can be detected, indicating good reversibility and rate capability. The nearly symmetric GCD curves of the ASC indicate its high columbic efficiency (Fig. 7c). From the GCD curves, the specific capacitance of the device is calculated and plotted in Fig. S25c. The device delivers a high specific capacitance of 180 F g^{-1} at a current density of 1 A g^{-1}, whereas 68 F g^{-1} is retained even at 10 A g^{-1}. The cycling stability was evaluated by successive GCD measurements at a high current density of 10 A g^{-1} (Fig. 7d). The result shows an excellent cycling performance with ~95.4% capacitance retention and excellent Coulombic efficiency of nearly 100% after 5000 cycles. In case of non-linear GCD characteristic of the present ASC device, the energy efficiency (η_E) would be considered as a key parameter to evaluate its potential practical applications [69]. The η_E is determined to be ~83.7% in the initial stage and still remains 82.5% after the cycling test (Fig. S26), which is superior to the recently reported value [69, 70]. The EIS plots of the device before and after cycling test are shown in Fig. S25d. The obtained R_s and R_{ct} of before cycling are 2.2 and 7.9 Ω, respectively. After cycling test, the device shows an increase in the value of R_s and R_{ct} compared to the original state, which is probably ascribed to the loss of adhesion of electrochemically active F-Co_2MnO_{4-x} and Fe_2O_3 with the CF current collector upon long□term cycling, resulting in the attenuated active material/current collector contact and charge-transfer kinetics. The Ragone plot of the F-Co_2MnO_{4-x}/CF//Fe_2O_3/CF associated with the relationship between energy density and power density is shown in Fig. 7e. A maximum gravimetric energy density of 64.4 W h kg^{-1} is achieved at a power density of 800 W kg^{-1}, and 24.2 W h kg^{-1} is

23

retained at a high power density of 8000 W kg^{-1}. These results are higher than those of quasi-solid-state asymmetrical electrochemical energy storage devices, such as NiCo$_2$O$_4$@CNT/CNT//carbon paper [71], ZnCo$_2$O$_4$//vanadium nitride [72], Co$_3$O$_4$//carbon aerogel [73], NiO//α-Fe$_2$O$_3$ [74], MnO$_2$/CNT//Fe$_2$O$_3$/CNT [75], and Co$_3$O$_4$@CoMoO$_4$//CNT [76]. For comparison, a quasi-solid-state symmetric supercapacitor was assembled with pristine CF substrate as the electrodes. The CV curves collected at different scan rates and GCD curves conducted at different discharge current densities for the CF//CF device are shown in Fig. S27a-c. The nearly rectangle-like CV curves and the quasi-isosceles triangle GCD curves of the CF//CF device indicate its electrical double layer capacitive properties. Notably, the CF//CF device exhibits a much low energy density of 0.97 W h kg^{-1} at a power density of 500 W h kg^{-1} due to its low specific capacitance and narrow cell voltage (Fig. S27d). Fig. 7f and 7g show no negligible change in the CV curves of the F-Co$_2$MnO$_{4-x}$/CF//Fe$_2$O$_3$/CF device at di□erent bending angles, implying its good mechanical flexibility. Moreover, the unitarity of good mechanical flexibility and cycling stability of the device was investigated. Notably, nearly 89.9% capacitance of the initial value is retained after 2000 cycles with a bending angle ranging from 0° to 30° by using the comparative CV curves at 10 mV s^{-1} (Fig. 7h). No significant change is observed in the EIS spectra (Fig. S28) of the F-Co$_2$MnO$_{4-x}$/CF//Fe$_2$O$_3$/CF device recorded under the different bending angles (0°, 30°, 60°, 90°), again demonstrating the excellent flexibility of the constructed device. To further demonstrate the potential of the device at a circuit level of real applications, we assembled two

24

$F-Co_2MnO_{4-x}/CF//Fe_2O_3/CF$ devices and connected them in series. Fig. 7i illustrates that the two tandem devices can power a red light-emitting diode (LED, ~2.0 V). The ASC device is charged to 1.6 V at a current density of 1 A g^{-1} and kept the constant-voltage charging at 1.6 V for 2 h, and then allowed to undergo self-discharge process. The self-discharge curve shows a rapid self-discharge rate within the first several hours, which then reduces slowly after several hours. Finally the output voltage drops to ~0.94 V with 58.8 % retention of the initial charge potential after 20 h (Fig. S29), indicating low self-discharge behaviour of our prepared devices.

3. Conclusion

An effective strategy of F-triggered and O-vacancy-mediated modulation for the synthesis of $F-Co_2MnO_{4-x}$ nanowires on a CF substrate is demonstrated. Insight into the effect of F doping and O vacancy on electrochemical performance of $F-Co_2MnO_{4-x}$ in supercapacitors is concluded by theoretical and experimental studies. The results reveal that the simultaneous introduction of F dopant and O vacancies to $F-Co_2MnO_{4-x}$ results in newly formed energy levels and increases the reactivity of electrochemically active sites, thereby significantly improving the electrochemical performance. The integrated design of nanowires anchored on a conductive substrate not only provides fast charge transport but also avoids the addition of conductive additives and binding agents. With good electrical conductivity and distinct structural advantages, the resultant $F-Co_2MnO_{4-x}/CF$ electrode yields a high specific capacity of

269 mA h g^{-1} at a current density of 1 A g^{-1} and an excellent cyclic stability with 93.2% retention over 5000 cycles 15 A g^{-1}. The fabricated quasi-solid-state ASC comprising F-Co$_2$MnO$_{4-x}$/CF and Fe$_2$O$_3$/CF electrodes exhibits a maximum energy density of 64.4 W h kg^{-1} at a power density of 800 W kg^{-1} and possesses highly integrative features of excellent mechanical flexibility and cycling performance (89.9% capacitance retention at 10 mV s^{-1} after 2000 cycles with a bending angle ranging from 0 to 30°). These findings offer new opportunities to tune the intrinsic structural properties of electroactive materials for their use as advanced electrodes in portable and flexible electronics.

4. Experimental Section

4.1 Synthesis of materials

Synthesis of F-Co$_2$MnO$_4$/CF. Prior to the experiment, the CF substrate was treated with concentrated HNO$_3$ solution for 40 min, and then rinsed by deionized (DI) water for several times. All the chemicals were directly used without further purification after purchase. In this procedure, 1.4 mmol of Mn(NO$_3$)$_2$·4H$_2$O, 2.8 mmol of Co(NO$_3$)$_2$·6H$_2$O, and 16.8 mmol urea [CO(NH$_2$)$_2$] were dissolved in a solution of 70 mL of DI water at room temperature to form a clear pink solution and added with 8.4 mmol of ammonium fluoride (NH$_4$F) under continuous stirring. Two pieces of cleaned CF (2.0 cm × 3.0 cm) were placed in the above solution, and then the solution was transferred to a Teflon-lined stainless steel autoclave and kept at 100 °C for 6 h. The substrate with the as-grown precursor was annealed in air at 350 °C for 2 h. For

26

the comparative study, pure Co_2MnO_4 was prepared without the added NH_4F under the same conditions. The loading mass of the as-synthesized products on the CF substrate was about 1.2 mg cm^{-2}.

Synthesis of F-Co$_2$MnO$_{4-x}$/CF. The obtained F-Co$_2$MnO$_4$ nanowires anchored on CF were immersed in a solution containing 30 mL of ethylene glycol ($C_2H_6O_2$) and 30 mmol of NaOH and transferred to a Teflon-lined stainless autoclave for solvothermal reaction at 120 °C for 14 h. Then, the substrate covered with F-Co$_2$MnO$_{4-x}$ was taken out, washed with DI water and ethanol, and dried at 70 °C for 12 h. The average mass loading of F-Co$_2$MnO$_{4-x}$ on CF substrate was about 1.1 mg cm^{-2}.

Synthesis of Fe$_2$O$_3$/CF. A hollow Fe_2O_3 core branched structure was fabricated through a self-sacrificing method as reported in literature with some modifications [66]. First, ZnO nanorods were vertically grown on a CF via modified wet chemical process [77]. A layer of ZnO crystal seeds was deposited on the substrate by immersing the CF in 0.5 M $KMnO_4$ for 40 mins. The seeded substrate was then immersed in a solution containing 10.5 mM $Zn(NO_3)_2 \cdot 6H_2O$, 10.5 mM hexamethylenetetramine, and 70 mL of DI water, added with ammonia water (4 mL; 30%), and kept at 90 °C for 12 h. Second, the obtained substrate with ZnO nanorods was immersed in 0.013 M $Fe(NO_3)_3$ aqueous solution and maintained at room temperature for 24 h. Finally, the obtained products were washed with DI water, dried in air, and annealed at 400 °C for 2 h under Ar. The load mass of Fe_2O_3 was about 1.1 mg cm^{-2}.

27

4.2 Material characterization

The morphological characteristics and structures of the samples were examined with a field-emission scanning electron microscope (FESEM; JEOL-7801) and a transmission electron microscope (TEM; JEOL, JEM-2010). The chemical composition and crystalline structures of the samples were evaluated through X-ray diffraction (XRD) on Rigaku Smartlab equipped with Cu Kα source ($\lambda = 1.5406$ Å). Raman spectra were recorded with a FluoroMax-4 (Horiba Jobin Yvon) spectrofluorometer. Electron paramagnetic resonance (EPR) spectra were obtained using a Bruker EMX-plus spectrometer equipped with a dual mode cavity operating at X-band frequencies (9.4 GHz) at room temperature. Surface chemical composition was analyzed through X-ray photoelectron spectroscopy (XPS; VG-Microtech ESCA-2000) with a monochromatic Al Kα X-ray source. The electrical properties of sample pellets compressed from as-synthesized powders were measured by a Keithley 4200□SCS semiconductor characterization system using a 4-probe method. The Brunauer–Emmett–Teller (BET) surface areas were determined with an Autosorb-iQ 2ST/MP (Quantachrome, USA) system using nitrogen as an adsorptive at 77 K. The bending test of the assembled ASC device was conducted on an Instron (Micro Tester, 5848, Instron) using continuous compression recovery process at a speed of 5 mm/s.

4.3 Electrochemical measurement

Electrochemical measurements were conducted with a multi-channel electrochemical analyzer (Ivium Technologies, Netherlands) in 1 M KOH electrolyte. For the three

electrode tests, the synthesized samples on the CF (area= 1×1 cm^2), the saturated calomel, and a Pt foil were used as the working electrode, the reference electrode, and the counter electrode, respectively. The loading masses of as-synthesized samples were determined by subtracting the weight of CF substrate before and after deposition of active materials. Specifically, the total mass (M_{total}) of active material loading on the piece of CF was obtained, and then the mass (m_{per}) of per unit area (1 cm^2) was calculated based on the equation: $m_{per} = M_{total}/6$. Two electrode tests were performed by assembling F-Co$_2$MnO$_{4-x}$ as the positive electrode and Fe$_2$O$_3$ as the negative electrode, with KOH/polyvinyl alcohol (PVA) as the solid electrolyte. The KOH/PVA electrolyte was prepared by dissolving 2 g of KOH and 2.4 g of PVA in 20 mL of DI water and heated at 90°C under stirring for 4 h.

Considering that Co$_2$MnO$_4$-based electrodes exhibit obvious Faradaic peaks and charge/discharge plateaus, it is reasonable for evaluating their charge storage performance using specific capacity [4]. While the CV and GCD curves of Fe$_2$O$_3$ electrode show dominantly pseudocapacitive behaviour rather than battery-type electrode behaviour due to the nanoscale structural feature of Fe$_2$O$_3$ [4]. Therefore, charge storage performance of Fe$_2$O$_3$ was evaluated using specific capacitance. The specific capacity Q (mA h g^{-1}) of Co$_2$MnO$_4$-based electrodes and the specific capacitance C_s (F g^{-1}) of Fe$_2$O$_3$ electrode can be calculated from the discharge curves by using the following equations [47, 78]:

$$Q = \frac{1}{3.6} \times \frac{I \int_{t_i}^{t_f} V dt}{m \times U_{mean}} = \frac{1}{3.6} \times \frac{I \int_{t_i}^{t_f} V dt}{m \times \frac{U}{2}} = \frac{1}{1.8} \times \frac{I \int_{t_i}^{t_f} V dt}{mU} \tag{6}$$

$$C_s = \frac{I \int_{t_i}^{t_f} V dt}{m \int_{V_i}^{V_f} V dV} \tag{7}$$

where I (A) is the current response, t_i and t_f are the initial and final values of discharge time t (s), m (g) is the mass, V (V) is the operating potential, U_{mean} (V) is the mean value of V, and U (V) is the potential window, V_i and V_f are the initial and final values of V (V) during discharge process, respectively.

Prior to the assembling of ASC device, the charge stored in the positive and negative electrodes should be balanced using the following relationship [4]:

$$\frac{m_+}{m_-} = \frac{C_- \times \Delta V_-}{Q_+} \tag{8}$$

where Q_+ (mA h g^{-1}) and C_- (F g^{-1}) are the gravimetric specific capacity of the positive electrode and specific capacitance of negative electrode, respectively. ΔV_- is the potential window of negative electrode material. m_+ and m_- (g) are the mass of the positive and negative electrodes, respectively.

For the assembled asymmetric supercapacitors, the specific capacitance (C_d; F g^{-1}), energy density (E; W h kg^{-1}), power density (P; W kg^{-1}) and energy efficiency (η_E) were calculated on the basis of the following equations [47, 69, 79]:

$$C_d = \frac{I \int_{t_i}^{t_f} V dt}{M \int_{V_i}^{V_f} V dV} \tag{9}$$

$$E = \frac{I \int_0^t V_s dt}{3.6 \cdot M} \tag{10}$$

$$P = \frac{3600 \times E}{t} \tag{11}$$

$$\eta_E = \frac{E_D}{E_C} \tag{12}$$

30

where M (g) is the total mass of positive and negative electrode materials, V_s (V) is the operating voltage, U_s(V) is the voltage window, and E_C and E_D are the charge and discharge specific energies (E), respectively.

4.4 DFT calculations

Density functional theory (DFT) calculations were performed at the spin-polarized GGA+U and PBE level by using the Vienna ab initio simulation package [80, 81]. Core ion and valence electron interaction was described in accordance with the projector augmented wave method [82]. The valence electronic configurations of Co, Mn, O, and F elements in this study are $3d^7 4s^2$, $3d^5 4s^2$, $2s^2 2p^4$, and $2s^2 2p^5$, respectively. Therefore, the numbers of valence electrons for Co, Mn, O, and F are 9, 7, 6, and 7, respectively. A cutoff energy of 600 eV was used to expand the plane waves. The effective onsite Coulomb terms (U values) for the $3d$ states of Mn and Co were set as 4.5 and 3.91 eV, respectively [83, 84]. The Co_2MnO_4 was modeled with its conventional unit-cell, which contains 8 Mn, 16 Co and 32 O atoms. A $3 \times 3 \times 3$ Monkhorst-Pack scheme k-point mesh was used for structural optimization and the density of states (DOS) [85], which was smeared by the Gaussian smearing method with a smearing width of 0.05 eV. The lattice constants and the atomic positions were fully relaxed until the final forces were converged to 0.05 eV/Å. Although this force convergence criterion seems coarse, we mention here that the ground state energy is converged to less than 1 meV per formula unit. The inverse spinel structure of Co_2MnO_4 is much more thermodynamically stable than its standard spinel structure [58]. As such, an inverse spinel model was used in the current study.

31

Supporting Information

Supporting Information is available from the Elsevier eLibrary or from the author.

Conflicts of **interest**

The authors declare there are no conflicts of interest.
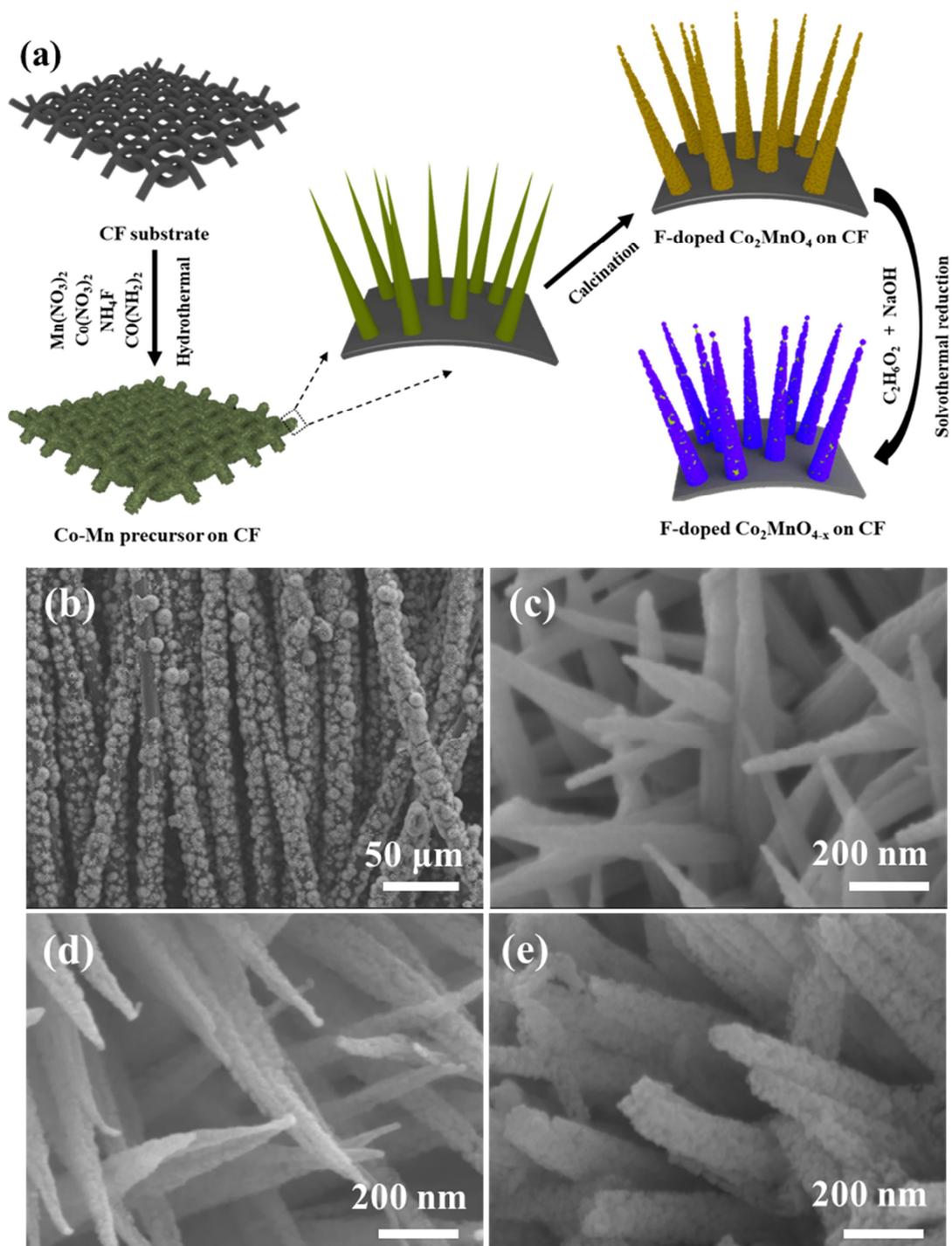
Fig. 1. (a) Schematic of the synthesis of F-Co$_2$MnO$_{4-x}$ nanowires on CF substrate.

SEM images of (b, c) Co-Mn precursor, (d) F-Co$_2$MnO$_4$, and (e) F-Co$_2$MnO$_{4-x}$.
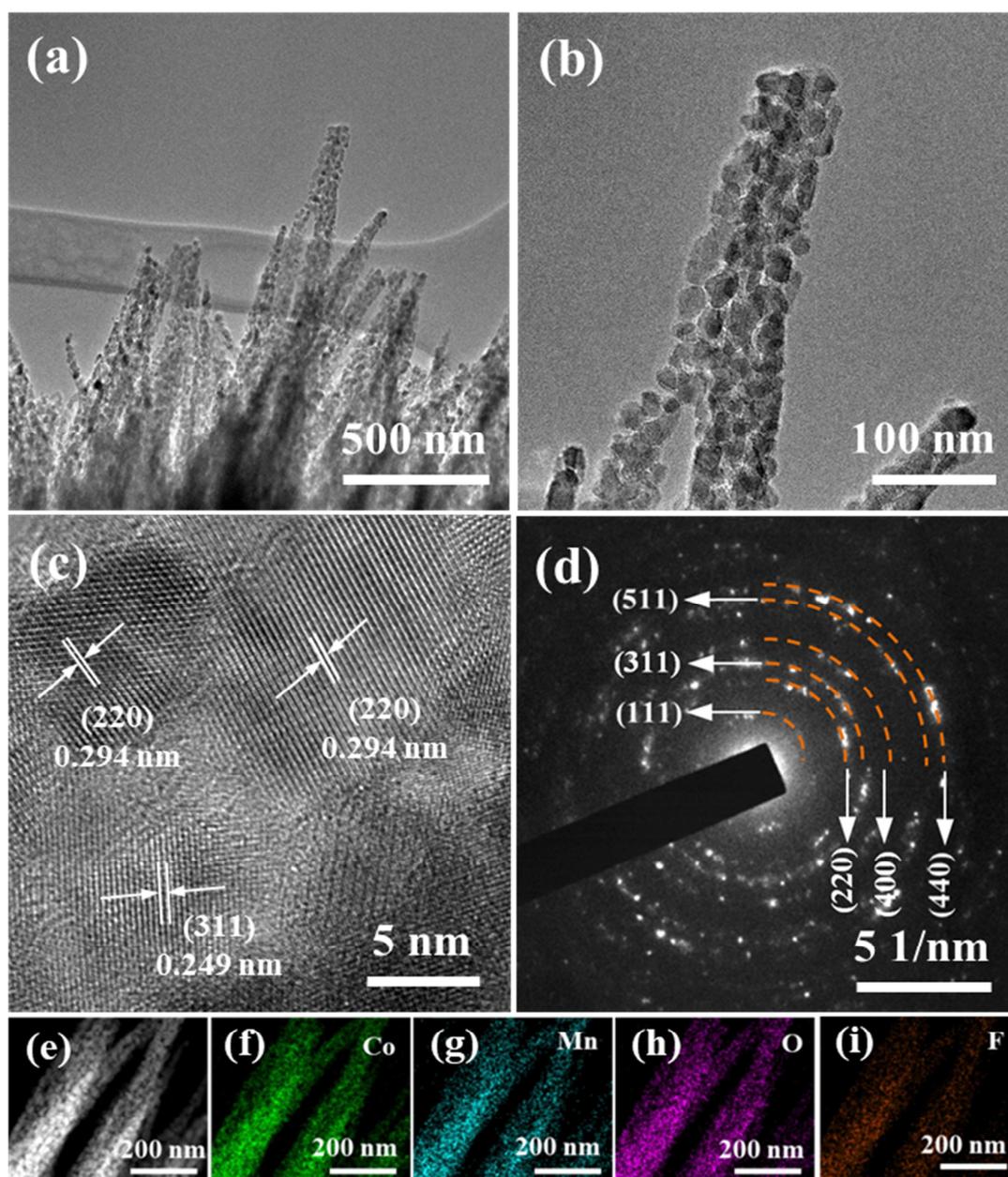
Fig. 2. (a, b) TEM images, (c) HRTEM image, (d) SAED pattern, and (e–i) STEM-EDS elemental mappings of Co, Mn, O, and F of the prepared F-Co$_2$MnO$_{4-x}$.
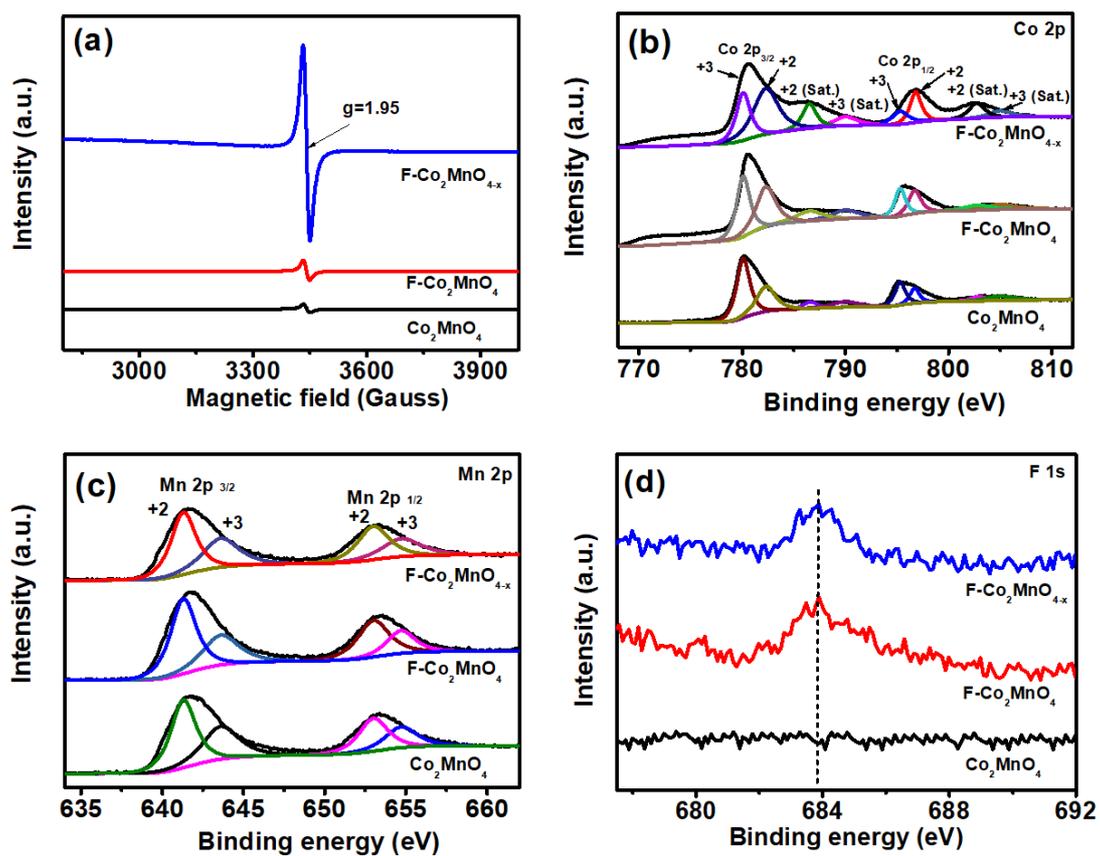
Fig. 3. (a) EPR spectra and high-resolution (b) Co 2p, (c) Mn 2p, and (d) F 1s XPS

spectra of the as-synthesized Co_2MnO_4, $F-Co_2MnO_4$, and $F-Co_2MnO_{4-x}$.
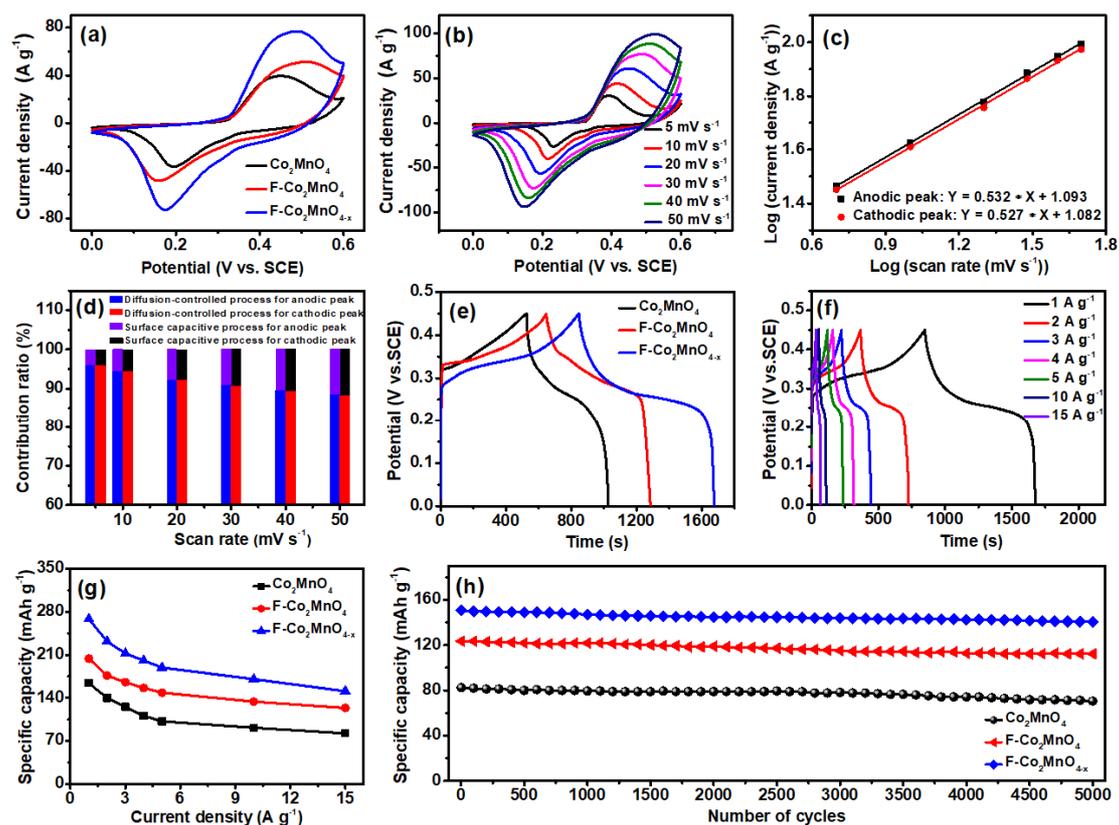
Fig. 4. (a) Comparative CV curves of Co_2MnO_4, $F-Co_2MnO_4$, and $F-Co_2MnO_{4-x}$ electrodes at a scan rate of 30 mV s^{-1}. (b) CV curves of $F-Co_2MnO_{4-x}$ at different scan rates ranging from 5 mV s^{-1} to 50 mV s^{-1}. (c) b determination from the plot of log(i) versus log(v) for both cathodic and anodic peaks of $F-Co_2MnO_{4-x}$. (d) Percentage contribution to the total charge from the capacitive and diffusion-controlled processes of $F-Co_2MnO_{4-x}$ at different scan rates. (e) GCD curves of Co_2MnO_4, $F-Co_2MnO_4$, and $F-Co_2MnO_{4-x}$ electrodes at a current density of 1 A g^{-1}. (f) GCD curves of $F-Co_2MnO_{4-x}$ at different current densities. (g) Comparison of the specific capacities as a function of current density for Co_2MnO_4, $F-Co_2MnO_4$, and $F-Co_2MnO_{4-x}$ electrodes. (h) Capacity retentions of Co_2MnO_4, $F-Co_2MnO_4$, and $F-Co_2MnO_{4-x}$ electrodes at a current density of 15 A g^{-1}.
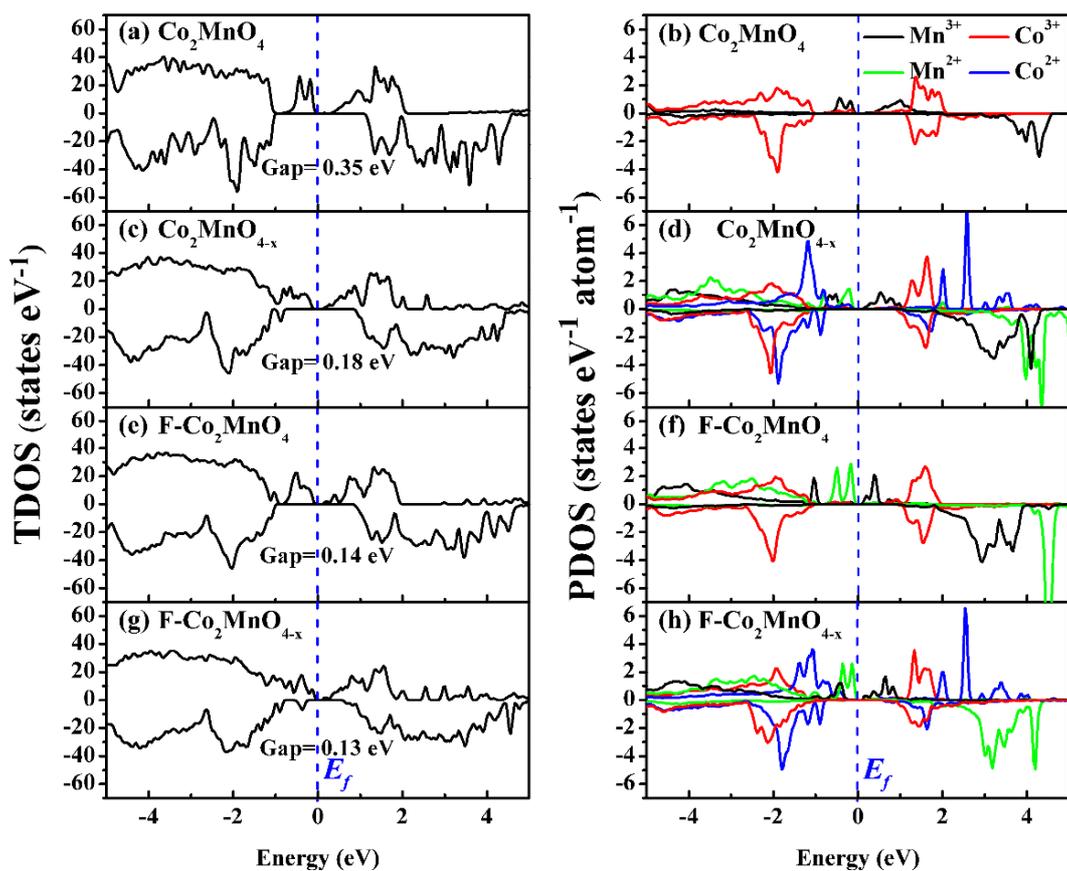
Fig. 5 Total (left) and partial (right) density of states of the inverse spinel Co_2MnO_4 (a, b), Co_2MnO_{4-x} (c, d), $F-Co_2MnO_4$ (e, f) and $F-Co_2MnO_{4-x}$ (g, h).
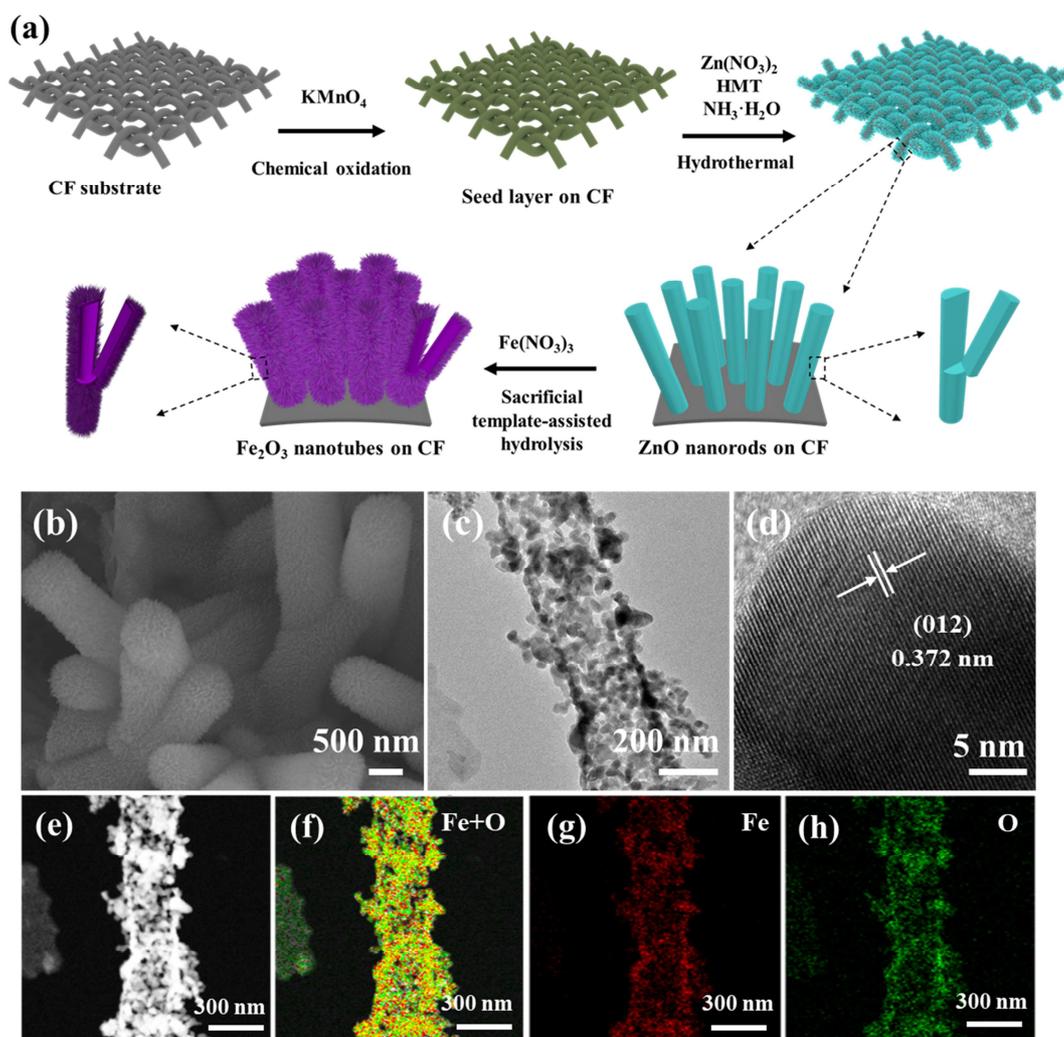
Fig. 6. (a) Synthesis scheme of the hollow Fe_2O_3 core-branch nanostructure. Electron

microscopy characterizations of Fe_2O_3 nanostructure; (b) SEM image; (c) TEM image;

(d) HRTEM image; (e–h) TEM image, and corresponding EDS elemental mapping.
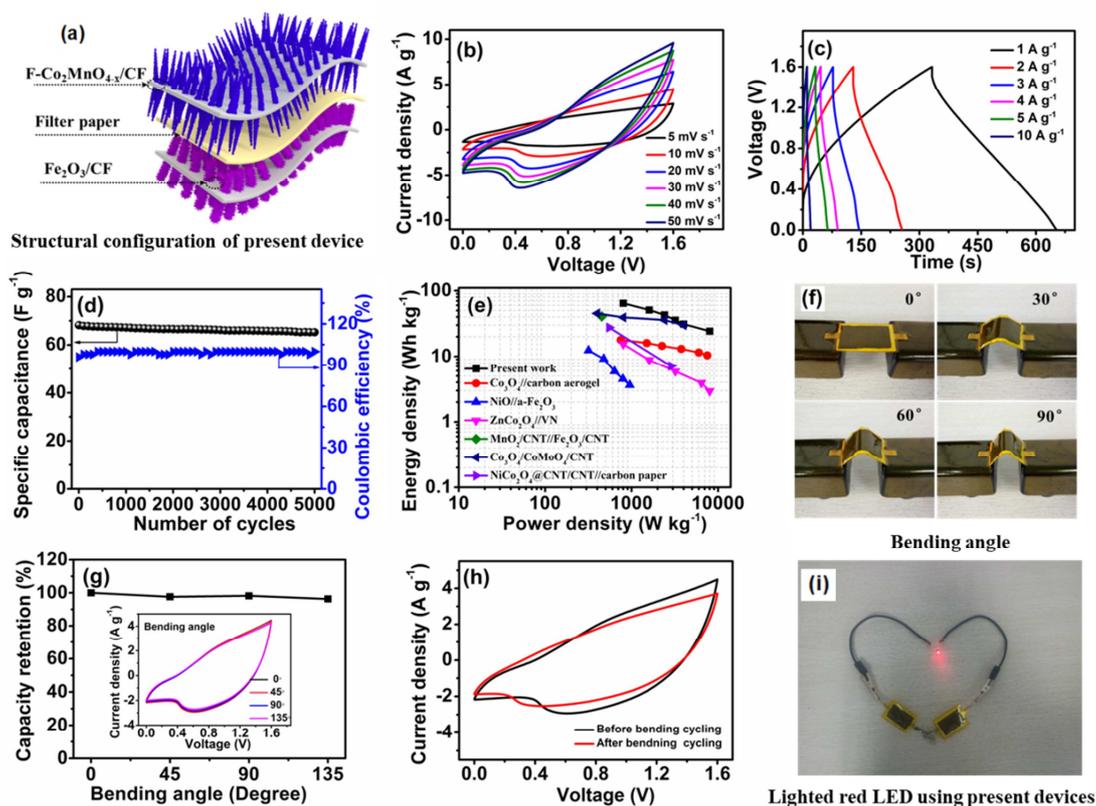
Fig. 7. Electrochemical properties of the assembled quasi-solid-state F-Co$_2$MnO$_{4-x}$/CF//Fe$_2$O$_3$/CF ASC. (a) Schematic of the structural configuration of the device. (b) CV curves obtained at different scan rates of 5–50 mV s^{-1}. (c) GCD curves at different current densities of 1–10 A g^{-1}. (d) Cycling performance and Coulombic efficiency at a current density of 10 A g^{-1}. (e) Ragone plot (power density vs. energy density). (f) Digital photographs of the device bent at different angles (0°, 30°, 60°, and 90°). (g) Capacitance retention; the inset shows the CV curves obtained at different bending angles. (h) CV curves obtained for the device before and after 2000 cycles at a scan rate of 10 mV s^{-1} under a bending angle of 0–30°. (i) A red LED illuminated by ASC devices connected in series.

Graphical abstract
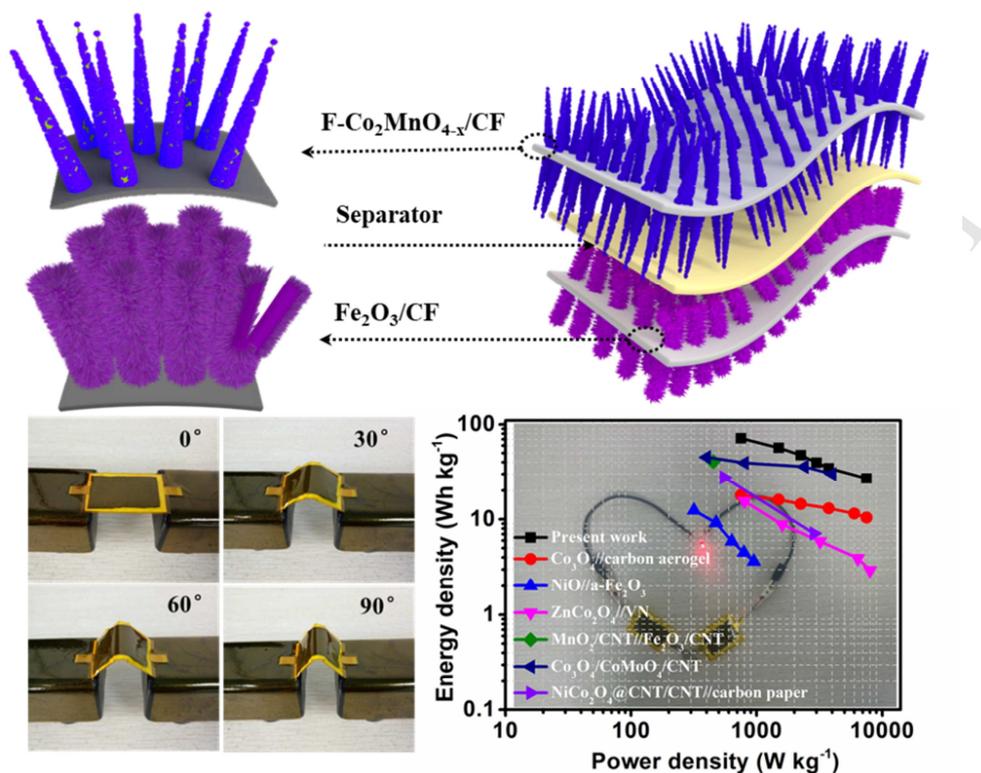
Fluorine-doped oxygen-deficient Co_2MnO_4 nanowires were fabricated on a flexible carbon fiber for use as electrode materials for supercapacitor. Experimental and theoretical studies provide new insight on the effect of the introduced F dopant and O vacancies on electrochemical performance of $F\text{-}Co_2MnO_{4\text{-}x}$. Flexible quasi-solid-state asymmetric supercapacitors comprising the $F\text{-}Co_2MnO_{4\text{-}x}$ as the positive electrode material and Fe_2O_3 as the negative electrode material achieve high energy density of 64.4 W h kg^{-1} at a power density of 800 W kg^{-1}, and highly integrative features with excellent cycling performance and mechanical flexibility (89.9% retention of the initial capacitance at 10 mV s^{-1} after 2000 bending cycles with an angle ranging from 0 to 30°).

References

[1] P. Huang, C. Lethien, S. Pinaud, K. Brousse, R. Laloo, V. Turq, M. Respaud, A. Demortiere, B. Daffos, P.-L. Taberna, Y. Gogotsi, P. Simon, On-chip and freestanding elastic carbon films for micro-supercapacitors, Science, 351 (2016) 691-695.

[2] J. Ye, H. Tan, S. Wu, K. Ni, F. Pan, J. Liu, Z. Tao, Y. Qu, H. Ji, P. Simon, Direct Laser Writing of Graphene Made from Chemical Vapor Deposition for Flexible, Integratable Micro-Supercapacitors with Ultrahigh Power Output, Adv. Mater., 30 (2018) 1801384.

[3] K. Landskron, Capacitance for Carbon Capture, Angew. Chem. Int. Ed., 57 (2018) 3548-3550.

[4] Y. Shao, M.F. El-Kady, J. Sun, Y. Li, Q. Zhang, M. Zhu, H. Wang, B. Dunn, R.B. Kaner, Design and Mechanisms of Asymmetric Supercapacitors, Chem. Rev., 118 (2018) 9233-9280.

[5] W. Zuo, R. Li, C. Zhou, Y. Li, J. Xia, J. Liu, Battery☐Supercapacitor Hybrid Devices: Recent Progress and Future Prospects, Adv. Sci., 4 (2017) 1600539.

[6] Y.-S. Hu, Batteries: getting solid, Nat. Energy, 1 (2016) 16042.

[7] W. Liu, M.S. Song, B. Kong, Y. Cui, Flexible and stretchable energy storage: recent advances and future perspectives, Adv. Mater., 29 (2017) 1603436.

[8] Y. Lin, Y. Gao, Z. Fan, Printable Fabrication of Nanocoral☐Structured Electrodes for High☐Performance Flexible and Planar Supercapacitor with Artistic Design, Adv. Mater., 29 (2017) 1701736.

[9] Z. Niu, W. Zhou, X. Chen, J. Chen, S. Xie, Highly Compressible and All☐Solid☐State Supercapacitors Based on Nanostructured Composite Sponge, Adv. Mater., 27 (2015) 6002-6008.

[10] Z. Cai, Y. Bi, E. Hu, W. Liu, N. Dwarica, Y. Tian, X. Li, Y. Kuang, Y. Li, X.Q. Yang, Single☐Crystalline Ultrathin Co_3O_4 Nanosheets with Massive Vacancy Defects for Enhanced Electrocatalysis, Adv. Energy Mater., 8 (2018) 1701694.

[11] W. Li, B. Zhang, R. Lin, S. Ho☐Kimura, G. He, X. Zhou, J. Hu, I.P. Parkin, A Dendritic Nickel Cobalt Sulfide Nanostructure for Alkaline Battery Electrodes, Adv. Funct. Mater., 28 (2018) 1705937.

[12] Y. Gogotsi, R.M. Penner, Energy Storage in Nanomaterials–Capacitive, Pseudocapacitive, or Battery-like?, ACS Nano, 12 (2018) 2081–2083.

[13] G. Liu, B. Wang, T. Liu, L. Wang, H. Luo, T. Gao, F. Wang, A. Liu, D. Wang, 3D self-supported hierarchical core/shell structured $MnCo_2O_4$@CoS arrays for high-energy supercapacitors, J. Mater. Chem. A, 6 (2018) 1822-1831.

41

[14] M. Yu, Z. Wang, C. Hou, Z. Wang, C. Liang, C. Zhao, Y. Tong, X. Lu, S. Yang, Nitrogen☐Doped Co_3O_4 Mesoporous Nanowire Arrays as an Additive☐Free Air☐ Cathode for Flexible Solid☐State Zinc–Air Batteries, Adv. Mater., 29 (2017) 1602868.

[15] K. Liang, K. Marcus, Z. Yang, L. Zhou, H. Pan, Y. Bai, Y. Du, M.H. Engelhard, Y. Yang, Freestanding NiFe Oxyfluoride Holey Film with Ultrahigh Volumetric Capacitance for Flexible Asymmetric Supercapacitors, Small, 14 (2018) 1702295.

[16] J. Xie, W. Liu, J. Xin, F. Lei, L. Gao, H. Qu, X. Zhang, Y. Xie, Dual Effect in Fluorine☐Doped Hematite Nanocrystals for Efficient Water Oxidation, ChemSusChem, 10 (2017) 4465-4471.

[17] M. Wang, Z. Li, C. Wang, R. Zhao, C. Li, D. Guo, L. Zhang, L. Yin, Novel Core–Shell $FeOF/Ni(OH)_2$ Hierarchical Nanostructure for All☐Solid☐State Flexible Supercapacitors with Enhanced Performance, Adv. Funct. Mater., 27 (2017) 1701014.

[18] W. Shi, R. Ding, X. Li, Q. Xu, D. Ying, Y. Huang, E. Liu, Bimetallic Co☐Mn Perovskite Fluorides as Highly☐Stable Electrode Materials for Supercapacitors, Chem. Eur. J, 23 (2017) 15305-15311.

[19] J. Wang, R. Gao, D. Zhou, Z. Chen, Z. Wu, G. Schumacher, Z. Hu, X. Liu, Boosting the Electrocatalytic Activity of Co_3O_4 Nanosheets for a $Li-O_2$ Battery through Modulating Inner Oxygen Vacancy and Exterior Co^{3+}/Co^{2+} Ratio, ACS Catal., 7 (2017) 6533-6541.

[20] S. Yang, Y. Liu, Y. Hao, X. Yang, W.A. Goddard, X.L. Zhang, B. Cao, Oxygen☐Vacancy Abundant Ultrafine Co_3O_4/Graphene Composites for High☐Rate Supercapacitor Electrodes, Adv. Sci., 5 (2018) 1700659.

[21] H.-S. Kim, J.B. Cook, H. Lin, J.S. Ko, S.H. Tolbert, V. Ozolins, B. Dunn, Oxygen vacancies enhance pseudocapacitive charge storage properties of MoO_{3-x}, Nat. Mater., 16 (2017) 454-460.

[22] X. Zou, A. Goswami, T. Asefa, Efficient noble metal-free (electro) catalysis of water and alcohol oxidations by zinc–cobalt layered double hydroxide, J Am Chem Soc., 135 (2013) 17242-17245.

[23] J. Yu, Q. Wang, D. O'Hare, L. Sun, Preparation of two dimensional layered double hydroxide nanosheets and their applications, Chem. Soc. Rev., 46 (2017) 5950-5974.

[24] Y. Wang, D. Yan, S. El Hankari, Y. Zou, S. Wang, Recent Progress on Layered Double Hydroxides and Their Derivatives for Electrocatalytic Water Splitting, Adv. Sci., 5 (2018) 1800064.

[25] P.S. Shinde, S.H. Choi, Y. Kim, J. Ryu, J.S. Jang, Onset potential behavior in α-Fe_2O_3 photoanodes: the influence of surface and diffusion Sn doping on the surface states, Phys. Chem. Chem. Phys., 18 (2016) 2495-2509.

[26] Y. Zhao, L. Hu, S. Zhao, L. Wu, Preparation of $MnCo_2O_4@Ni(OH)_2$ Core–Shell Flowers for Asymmetric Supercapacitor Materials with Ultrahigh Specific Capacitance, Adv. Funct. Mater., 26 (2016) 4085-4093.

[27] Y. Zhang, S. Liu, Y. Li, D. Deng, X. Si, Y. Ding, H. He, L. Luo, Z. Wang, Electrospun graphene decorated $MnCo_2O_4$ composite nanofibers for glucose biosensing, Biosens Bioelectron., 66 (2015) 308-315.

[28] C. Yan, G. Chen, X. Zhou, J. Sun, C. Lv, Template☐Based Engineering of Carbon☐Doped Co_3O_4 Hollow Nanofibers as Anode Materials for Lithium☐Ion Batteries, Adv. Funct. Mater., 26 (2016) 1428-1436.

[29] G.H. Lee, S. Lee, J.C. Kim, D.W. Kim, Y. Kang, D.W. Kim, $MnMoO_4$ Electrocatalysts for Superior Long☐Life and High☐Rate Lithium☐Oxygen Batteries, Adv. Energy Mater., 7 (2017) 1601741.

[30] B. Sambandam, R.J.V. Michael, P.T. Manoharan, Oxygen vacancies and intense luminescence in manganese loaded ZnO microflowers for visible light water splitting, Nanoscale, 7 (2015) 13935-13942.

[31] H. Liang, C. Xia, A.-H. Emwas, D.H. Anjum, X. Miao, H.N. Alshareef, Phosphine Plasma Activation of α-Fe_2O_3 for High Energy Asymmetric Supercapacitors, Nano Energy, 49 (2018) 155-162.

[32] X. Wei, Y. Li, H. Peng, D. Gao, Y. Ou, Y. Yang, J. Hu, Y. Zhang, P. Xiao, A novel functional material of Co_3O_4/Fe_2O_3 nanocubes derived from a MOF precursor for high-performance electrochemical energy storage and conversion application, Chem Eng J., 355 (2019) 336-340.

[33] H. Tan, Z. Liu, D. Chao, P. Hao, D. Jia, Y. Sang, H. Liu, H.J. Fan, Partial Nitridation☐Induced Electrochemistry Enhancement of Ternary Oxide Nanosheets for Fiber Energy Storage Device, Adv. Energy Mater., 8 (2018) 1800685.

[34] S. Wang, P. Chen, J.H. Yun, Y. Hu, L. Wang, An electrochemically treated $BiVO_4$ photoanode for efficient photoelectrochemical water splitting, Angew. Chem. Int. Ed., 56 (2017) 8500-8504.

[35] T.Y. Ma, Y. Zheng, S. Dai, M. Jaroniec, S.Z. Qiao, Mesoporous $MnCo_2O_4$ with abundant oxygen vacancy defects as high-performance oxygen reduction catalysts, J. Mater. Chem. A, 2 (2014) 8676-8682.

[36] Y. Lv, A. Liu, H. Che, J. Mu, Z. Guo, X. Zhang, Y. Bai, Z. Zhang, G. Wang, Z. Pei, Three-dimensional interconnected $MnCo_2O_4$ nanosheets@$MnMoO_4$ nanosheets core-shell nanoarrays on Ni foam for high-performance supercapacitors, Chem Eng J., 336 (2018) 64-73.

[37] D. Cui, Z. Zheng, X. Peng, T. Li, T. Sun, L. Yuan, Fluorine-doped SnO_2 nanoparticles anchored on reduced graphene oxide as a high-performance lithium ion battery anode, J. Power Sources, 362 (2017) 20-26.

43

[38] Y. Xue, Y. Wang, H. Liu, X. Yu, H. Xue, L. Feng, Electrochemical oxygen evolution reaction catalyzed by a novel nickel-cobalt–fluoride catalyst, Chemical Communications, 54 (2018) 6204-6207.

[39] M.K. Datta, K. Kadakia, O.I. Velikokhatnyi, P.H. Jampani, S.J. Chung, J.A. Poston, A. Manivannan, P.N. Kumta, High performance robust F-doped tin oxide based oxygen evolution electro-catalysts for PEM based water electrolysis, J. Mater. Chem. A, 1 (2013) 4026-4037.

[40] Y. Ma, B. Ding, G. Ji, J.Y. Lee, Carbon-encapsulated F-doped $Li_4Ti_5O_{12}$ as a high rate anode material for Li^+ batteries, ACS Nano, 7 (2013) 10870-10878.

[41] L. Ma, S. Chen, Z. Pei, H. Li, Z. Wang, Z. Liu, Z. Tang, J.A. Zapien, C. Zhi, Flexible Waterproof Rechargeable Hybrid Zinc Batteries Initiated by Multifunctional Oxygen Vacancies-Rich Cobalt Oxide, ACS nano, 12 (2018) 8597-8605.

[42] Y. Xu, X. Wang, C. An, Y. Wang, L. Jiao, H. Yuan, Facile synthesis route of porous $MnCo_2O_4$ and $CoMn_2O_4$ nanowires and their excellent electrochemical properties in supercapacitors, J. Mater. Chem. A, 2 (2014) 16480-16488.

[43] L. Li, Y. Zhang, X. Liu, S. Shi, X. Zhao, H. Zhang, X. Ge, G. Cai, C. Gu, X. Wang, One-dimension $MnCo_2O_4$ nanowire arrays for electrochemical energy storage, Electrochimica Acta, 116 (2014) 467-474.

[44] A. Pendashteh, S.E. Moosavifard, M.S. Rahmanifar, Y. Wang, M.F. El-Kady, R.B. Kaner, M.F. Mousavi, Highly ordered mesoporous $CuCo_2O_4$ nanowires, a promising solution for high-performance supercapacitors, Chem. Mater., 27 (2015) 3919-3926.

[45] L. Sheng, L. Jiang, T. Wei, Q. Zhou, Y. Jiang, Z. Jiang, Z. Liu, Z. Fan, $Fe(CN)_6^{3-}$ ion-modified MnO_2/graphene nanoribbons enabling high energy density asymmetric supercapacitors, J. Mater. Chem. A, 8 (2018) 7649-7658.

[46] I.E. Rauda, V. Augustyn, B. Dunn, S.H. Tolbert, Enhancing pseudocapacitive charge storage in polymer templated mesoporous materials, Acc Chem Res., 46 (2013) 1113-1124.

[47] S. Liu, Y. Yin, K.S. Hui, K.N. Hui, S.C. Lee, S.C. Jun, High‐Performance Flexible Quasi‐Solid‐State Supercapacitors Realized by Molybdenum Dioxide@ Nitrogen‐Doped Carbon and Copper Cobalt Sulfide Tubular Nanostructures, Adv. Sci., 5 (2018) 1800733.

[48] J. Lin, H. Wang, Y. Yan, X. Zheng, H. Jia, J. Qi, J. Cao, J. Tu, W. Fei, J. Feng, Core-branched $CoSe_2$/$Ni_{0.85}Se$ nanotube arrays on Ni foam with remarkable electrochemical performance for hybrid supercapacitors, J. Mater. Chem. A, 6 (2018) 19151-19158.

[49] P. Simon, Y. Gogotsi, B. Dunn, Where do batteries end and supercapacitors begin?, Science, 343 (2014) 1210-1211.

[50] L. Kuang, F. Ji, X. Pan, D. Wang, X. Chen, D. Jiang, Y. Zhang, B. Ding, Mesoporous $MnCo_2O_{4.5}$ nanoneedle arrays electrode for high-performance asymmetric supercapacitor application, Chem Eng J., 315 (2017) 491-499.

[51] A.K. Mondal, D. Su, S. Chen, A. Ung, H.S. Kim, G. Wang, Mesoporous $MnCo_2O_4$ with a Flake☐Like Structure as Advanced Electrode Materials for Lithium☐Ion Batteries and Supercapacitors, Chem. Eur. J, 21 (2015) 1526-1532.

[52] J. Xu, Y. Sun, M. Lu, L. Wang, J. Zhang, E. Tao, J. Qian, X. Liu, Fabrication of the porous $MnCo_2O_4$ nanorod arrays on Ni foam as an advanced electrode for asymmetric supercapacitors, Acta Mater., 152 (2018) 162-174.

[53] P. Pachfule, D. Shinde, M. Majumder, Q. Xu, Fabrication of carbon nanorods and graphene nanoribbons from a metal–organic framework, Nat Chem., 8 (2016) 718.

[54] Y. Jiao, J. Pei, D. Chen, C. Yan, Y. Hu, Q. Zhang, G. Chen, Mixed-metallic MOF based electrode materials for high performance hybrid supercapacitors, J. Mater. Chem. A, 5 (2017) 1094-1102.

[55] S. Liu, K.V. Sankar, A. Kundu, M. Ma, J.-Y. Kwon, S.C. Jun, Honeycomb-like Interconnected Network of Nickel Phosphide Hetero-nanoparticles with Superior Electrochemical Performance for Supercapacitors, ACS Appl. Mater. Interfaces, 9 (2017) 21829–21838.

[56] Y. Wang, Y. Lei, J. Li, L. Gu, H. Yuan, D. Xiao, Synthesis of 3D-nanonet hollow structured Co_3O_4 for high capacity supercapacitor, ACS Appl. Mater. Interfaces, 6 (2014) 6739-6747.

[57] Y. Li, M. Wu, C. Ouyang, The structural and electronic properties of spinel $MnCo_2O_4$ bulk and low-index surfaces: From first principles studies, Appl. Surf. Sci., 349 (2015) 510-515.

[58] S. Liu, D. Ni, H.-F. Li, K.N. Hui, C.-Y. Ouyang, S.C. Jun, Effect of cation substitution on the pseudocapacitive performance of spinel cobaltite MCo_2O_4 (M= Mn, Ni, Cu, and Co), J. Mater. Chem. A, 6 (2018) 10674-10685.

[59] R. Arras, T.L. Le, S. Guillemet-Fritsch, P. Dufour, C. Tenailleau, First-principles electronic structure calculations for the whole spinel oxide solid solution range $Mn_xCo_{3-x}O_4$ ($0 \leq x \leq 3$) and their comparison with experimental data, Phys. Chem. Chem. Phys., 18 (2016) 26166-26176.

[60] J. Shi, K. Lei, W. Sun, F. Li, F. Cheng, J. Chen, Synthesis of size-controlled $CoMn_2O_4$ quantum dots supported on carbon nanotubes for electrocatalytic oxygen reduction/evolution, Nano Res., 10 (2017) 3836-3847.

[61] J. Zheng, Z. Lei, Incorporation of CoO nanoparticles in 3D marigold flower-like hierarchical architecture $MnCo_2O_4$ for highly boosting solar light photo-oxidation and reduction ability, Appl Catal B., 237 (2018) 1-8.

[62] S. Shibli, P. Arun, A.V. Raj, Exploration of octahedrally shaped $MnCo_2O_4$ catalyst particles for visible light driven photocatalytic water splitting reaction, RSC Adv., 5 (2015) 19393-19399.

[63] T. Zhai, S. Xie, M. Yu, P. Fang, C. Liang, X. Lu, Y. Tong, Oxygen vacancies enhancing capacitive properties of MnO_2 nanorods for wearable asymmetric supercapacitors, Nano Energy, 8 (2014) 255-263.

[64] Y. Zeng, Z. Lai, Y. Han, H. Zhang, S. Xie, X. Lu, Oxygen☐Vacancy and Surface Modulation of Ultrathin Nickel Cobaltite Nanosheets as a High☐Energy Cathode for Advanced Zn☐Ion Batteries, Adv. Mater., 30 (2018) 1802396.

[65] J.Y. Kim, J.W. Jang, D.H. Youn, G. Magesh, J.S. Lee, A Stable and efficient hematite photoanode in a neutral electrolyte for solar water splitting: towards stability engineering, Adv. Energy Mater., 4 (2014) 1400476.

[66] L. Wang, H. Yang, X. Liu, R. Zeng, M. Li, Y. Huang, X. Hu, Constructing Hierarchical Tectorum☐like α☐Fe_2O_3/PPy Nanoarrays on Carbon Cloth for Solid☐State Asymmetric Supercapacitors, Angew. Chem. Int. Ed., 129 (2017) 1125-1130.

[67] Y. Li, J. Xu, T. Feng, Q. Yao, J. Xie, H. Xia, Fe_2O_3 Nanoneedles on Ultrafine Nickel Nanotube Arrays as Efficient Anode for High☐Performance Asymmetric Supercapacitors, Adv. Funct. Mater., 27 (2017) 1606728

[68] H. Quan, B. Cheng, Y. Xiao, S. Lei, One-pot synthesis of α-Fe_2O_3 nanoplates-reduced graphene oxide composites for supercapacitor application, Chem Eng J., 286 (2016) 165-173.

[69] A. Laheäär, P. Przygocki, Q. Abbas, F. Béguin, Appropriate methods for evaluating the efficiency and capacitive behavior of different types of supercapacitors, Electrochem commun., 60 (2015) 21-25.

[70] C.-C. Hu, J.-C. Chen, K.-H. Chang, Cathodic deposition of $Ni(OH)_2$ and $Co(OH)_2$ for asymmetric supercapacitors: importance of the electrochemical reversibility of redox couples, J. Power Sources, 221 (2013) 128-133.

[71] P. Wu, S. Cheng, M. Yao, L. Yang, Y. Zhu, P. Liu, O. Xing, J. Zhou, M. Wang, H. Luo, A Low☐Cost, Self☐Standing $NiCo_2O_4$@CNT/CNT Multilayer Electrode for Flexible Asymmetric Solid☐State Supercapacitors, Adv. Funct. Mater., 27 (2017) 1702160.

[72] J. Zhao, C. Li, Q. Zhang, J. Zhang, X. Wang, Z. Lin, J. Wang, W. Lv, C. Lu, C.-p. Wong, An all-solid-state, lightweight, and flexible asymmetric supercapacitor based on cabbage-like $ZnCo_2O_4$ and porous VN nanowires electrode materials, J. Mater. Chem. A, 5 (2017) 6928-6936.

[73] W. Liu, X. Li, M. Zhu, X. He, High-performance all-solid state asymmetric supercapacitor based on Co_3O_4 nanowires and carbon aerogel, J. Power Sources, 282 (2015) 179-186.

[74] S. Zhang, B. Yin, Z. Wang, F. Peter, Super long-life all solid-state asymmetric supercapacitor based on NiO nanosheets and α-Fe_2O_3 nanorods, Chem Eng J., 306 (2016) 193-203.

[75] T. Gu, B. Wei, High-performance all-solid-state asymmetric stretchable supercapacitors based on wrinkled MnO_2/CNT and Fe_2O_3/CNT macrofilms, J. Mater. Chem. A, 4 (2016) 12289-12295.

[76] J. Wang, X. Zhang, Q. Wei, H. Lv, Y. Tian, Z. Tong, X. Liu, J. Hao, H. Qu, J. Zhao, 3D self-supported nanopine forest-like Co_3O_4@$CoMoO_4$ core–shell architectures for high-energy solid state supercapacitors, Nano Energy, 19 (2016) 222-233.

[77] P. Yang, X. Xiao, Y. Li, Y. Ding, P. Qiang, X. Tan, W. Mai, Z. Lin, W. Wu, T. Li, Hydrogenated ZnO core–shell nanocables for flexible supercapacitors and self-powered systems, ACS Nano, 7 (2013) 2617-2626.

[78] L.-Q. Mai, A. Minhas-Khan, X. Tian, K.M. Hercule, Y.-L. Zhao, X. Lin, X. Xu, Synergistic interaction between redox-active electrolyte and binder-free functionalized carbon for ultrahigh supercapacitor performance, Nat. Commun., 4 (2013) 2923.

[79] S. Surendran, S. Shanmugapriya, A. Sivanantham, S. Shanmugam, R. Kalai Selvan, Electrospun Carbon Nanofibers Encapsulated with NiCoP: A Multifunctional Electrode for Supercapattery and Oxygen Reduction, Oxygen Evolution, and Hydrogen Evolution Reactions, Adv. Energy Mater., 8 (2018) 1800555.

[80] S. Dudarev, G. Botton, S. Savrasov, C. Humphreys, A. Sutton, Electron-energy-loss spectra and the structural stability of nickel oxide: An LSDA+ U study, Phys. Rev. B, 57 (1998) 1505.

[81] J.P. Perdew, M. Ernzerhof, K. Burke, Rationale for mixing exact exchange with density functional approximations, J. Chem. Phys., 105 (1996) 9982-9985.

[82] G. Kresse, G. Kresse and D. Joubert, From ultrasoft pseudopotentials to the projector augmented-wave method, Phys. Rev. B, 59 (1999) 1758.

[83] I. Solovyev, P. Dederichs, V. Anisimov, Corrected atomic limit in the local-density approximation and the electronic structure of d impurities in Rb, Phys. Rev. B, 50 (1994) 16861.

[84] G. Trimarchi, N. Binggeli, Structural and electronic properties of $LaMnO_3$ under pressure: An ab initio LDA+ U study, Phys. Rev. B, 71 (2005) 035101.

[85] H.J. Monkhorst, J.D. Pack, Special points for Brillouin-zone integrations, Phys. Rev. B, 13 (1976) 5188.